Modified Horton's infiltration model integrated with a Sub-Grid shallow water equation solver for High-Resolution flooding simulation

Saha, Abhishek; Stelling, Guus; Vuik, Cornelis

DOI
10.1016/j.jhydrol.2025.133326

Publication date
2025

Document Version
Final published version

Published in
Journal of Hydrology

Journal of Hydrology 660 (2025) 133326

Contents lists available at ScienceDirect

Journal of Hydrology

journal homepage: www.elsevier.com/locate/jhydrol

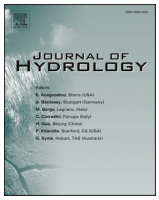

Modified Horton's infiltration model integrated with a Sub-Grid shallow water equation solver for High-Resolution flooding simulation

Abhishek Saha [a,b,*], Guus Stelling [a,c], Cornelis Vuik [a]

[a] Delft University of Technology, 2628 CD Delft, The Netherlands
[b] Hydroinformatics Institute, Singapore 118256 Singapore
[c] Stelling Hydraulics B.V., 1621 ME Hoorn, The Netherlands

ARTICLE INFO

This manuscript was handled by Corrado Corradini, Editor-in-Chief, with the assistance of Simone Di Prima, Associate Editor

Keywords:
Horton infiltration model
SWMM
Shallow water equations
Sub-grid
Rainfall-runoff
Numerical integration

ABSTRACT

Infiltration models are crucial components of rainfall-runoff models based on shallow water equations, combined with direct-rainfall for flooding simulations. While the original Horton's model is frequently used, various modifications have been proposed to deal with its limitations for intermittent rainfall patterns. We evaluate two modifications, from well-known Storm Water Management Model or SWMM and from Diskin and Nazimov, against the original Horton's model both theoretically and with numerical experiments. We find the formulation from Diskin and Nazimov as most suitable for real-world applications. In this paper, we describe an adaptation of the Diskin and Nazimov infiltration model through a Surface Detention Box model to integrate it into a shallow water equation solver, that accounts for detailed topographic information using a sub-grid approach. The Surface Detention Box model in this paper is generalized to account for sources and sinks other than infiltration. We verify the efficiency of our implementation for a catchment in Australia with intermittent and extreme rainstorms. We also demonstrate the accuracy, efficiency and the precise volume conservation of our method for high-resolution grids and large computational time steps, enabled by the predictor–corrector solver. In conclusion, we present a robust and efficient scheme for practical flood simulations, including various sources and sinks such as rainfall and infiltration. Our approach is a strong foundation for operational flood forecasting with high resolution Digital Terrain Models.

1. Introduction

Infiltration is a critical component of rainfall-runoff. Accurate representation of infiltration within rainfall-runoff models is paramount for reliable surface flood simulations (Gabellani et al., 2008). Urbanization, known to reduce infiltration capacity, leads to increased runoff and subsequent flooding during rainfall events. This phenomenon has prompted the development of concepts like the "sponge city" (Jiang, 2018; Shun, 2018) and numerous mitigation measures (Pearlmutter, 2021). Rainfall, land-use, soil texture and soil moisture conditions are factors affecting infiltration that vary spatiotemporally. While infiltration can be simulated by the Richards' equation (Richards, 1931), it is computationally expensive and requires detailed data of soil properties that are not readily available for practical modelling activities (Aron, 1992). Consequently, researchers have developed simplified infiltration models for various conditions (Assouline, 2013; Morbidelli et al., 2018).

Large-scale rainfall-runoff models for flood prediction require computational efficiency, particularly when implementing direct-rainfall or rain-on-grid methods in conjunction with two-dimensional shallow water equations (SWE) or their simplified variants (Godara et al., 2024) on high resolution digital terrain models (DTM). SCS-CN (Soil Conservation Service Curve Number) model, developed by the United States Department of Agriculture (Mishra and Singh, 2003), Green-Ampt (GA) model (Green and Ampt, 1911) and Horton's model (Horton, 1941), are used quite often by model developers (Aureli et al.,. 2020; Fernández-Pato et al., 2016; García-Feal et al.,. 2018; Gülbaz et al.,. 2020; Parnas et al.,. 2021; Peng et al.,. 2023) and practitioners due to their simplicity and established empirical parameters (Gabellani et al., 2008; Rawls et al., 1983). The SCS-CN method and Horton's method are widely used for computational efficiency since they do not require iterative computations to estimate infiltration rates. The full GA model requires iterations that may be avoided by using explicit approximations (Ni et al., 2020).

In order to estimate infiltration accurately for large scale rainfall-

* Corresponding author at: Delft University of Technology, 2628 CD Delft, the Netherlands.
E-mail address: a.saha@tudelft.nl (A. Saha).

https://doi.org/10.1016/j.jhydrol.2025.133326
Received 25 December 2024; Received in revised form 29 March 2025; Accepted 14 April 2025
Available online 21 April 2025

runoff/flooding simulations, the infiltration model should consider a couple of conditions: (i) rainfall with multiple peaks and intermittent low or dry periods (Bauer, 1974) and (ii) run-on or re-infiltration (Li, 2022), where infiltration is not only dependent on rainfall but also on runoff from adjacent areas. SCS-CN method has limitations to simulate these conditions (Michel et al., 2005). Modified Green-Ampt models (Chu and Mariño, 2005; Corradini et al.,. 1994) and Fractional Order GA model (Fernández-Pato et al., 2018) have been derived to allow simulation of rainstorms with multiple peaks over a longer duration. GA model has also been combined with SCS-CN model to estimate runoff (Li et al., 2015).

This study starts with Horton's model (Horton, 1941). It is regularly integrated with SWE (Fernández-Pato et al., 2016; Vallés, 2024) but suffers from drawbacks related to rainfall with intermittent dry-wet periods. Multiple modified Horton models (Aron, 1992; Bauer, 1974; Green, 1986; Shao and Baumgartl, 2016; Van Der Molen, 1986; Verma, 1982; Wang and Chu,. 2020; Yang et al., 2020) have been proposed that are more accurate than the classical Horton's model since the infiltration capacity depends on the infiltrated amount of water rather than time only. Some versions, such as in SWMM (Rossman, 2015), contain an option for the recovery of the infiltration capacity, and have proven to be effective in simulating flooding (Fernández-Pato et al., 2016) and flood mitigation strategies such as permeable pavement (Song, 2023), bioretention basins (Wang et al., 2021) and sponge city characteristics (Yang et al., 2023). However, the modified Horton model in SWMM requires iterative solutions.

Diskin and Nazimov's model (Diskin and Nazimov, 1995; Diskin and Nazimov, 1996), referred to as DNm here, is based on the principles of Horton's model, as demonstrated in (Diskin and Nazimov, 1995). It has been applied in mountainous catchments under various climatic conditions for runoff predictions with hydrological models (Fujimura et al., 2014; Fujimura et al., 2015) and semi-distributed flash flood models (Gabellani et al., 2008). DNm can be considered equivalent to the modified Horton model in SWMM since it includes recovery of infiltration capacity. For rainfall less than the minimum infiltration capacity, DNm produces more realistic restoration of infiltration capacity. Although modified Horton's models have been applied to SWE solvers (Parnas et al.,. 2021), the DNm formulation has not been integrated to 2D SWE solvers in current literature, to the best of our knowledge.

To achieve large gains in simulation speed for high resolution flooding simulations, sub-grid SWE models have been developed (Bates, 2000; Casulli, 2009). Sub-grid representation of topography at coarse computational grids allows accurate computation of volumes and water depths at significantly less computational costs (Stelling, 2012). For runoff calculations, we integrate DNm with a highly efficient sub-grid SWE-solver with a special approach for thin-layered overland flow on slopes (Stelling,. 2022). The integrated formulation with DNm and SWE presented here, referred to as DNm-SWE, can be used for watershed scale high-resolution simulations with arbitrary rainfall conditions, spatial heterogeneity of infiltration including run-on, in a computationally efficient manner.

The paper is structured as follows:

Section 2 introduces the surface detention box model (SDB) for ponding or drying, depending on its sources and sinks. Rain is a source term while infiltration acts as a sink term but also evapotranspiration (Viessman and Lewis, 2003) can be a sink. SDB is our alternative for the "regulating element" of DNm (Diskin and Nazimov, 1995). SDB not only improves DNm but also enables smooth integration of infiltration with SWE-solvers.

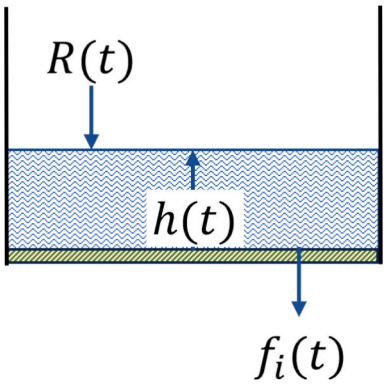

Fig. 1. Schematic of the Surface Detention Box (SDB) to connect infiltration models to the dynamic shallow water equation solver.

Section 3 compares three Horton parameter-based infiltration models (Horton's model, SWMM, and DNm). We find that from the three models, DNm integrated with SDB is the most versatile and efficient option for ponding and infiltration simulations.

Section 4 describes DNm integration with a SWE-solver for rainfall-runoff. A volume corrector is used with intrinsic flooding and drying due to guaranteed positive water depths, regardless the time step size. We present rainfall-runoff examples with infiltration, including a real-world flooding case.

Section 5 concludes this paper.

Finally, in two brief appendices some aspects of our proposed DNm-SWE are mathematically analysed. A third appendix presents an overview of the complete method with pseudo code and simple equations for a 3 grid-point example.

2. Surface Detention Box Model

In textbooks on hydrology (Viessman and Lewis, 2003), infiltration $f_i(t)$ is given by $f_i(t) = min\left[f_p(t), R(t)\right]$. Where $f_p(t)$ denotes infiltration capacity [Length/Time] and $R(t)$ the rainfall intensity [Length/Time]. For this formulation the infiltration stops as soon as the rain stops. But the available amount of water at the surface is the actual source of infiltration. Therefore, we have replaced this formulation with a simple box model, named: Surface Detention Box model, or SDB shown in Fig. 1.

We can derive the following equation:

$$\frac{dV}{dt} = A_h R(t) - A_h f_i(t), \frac{dV}{dt} = \frac{dV}{dh}\frac{dh}{dt} = A_h \frac{dh}{dt} \quad \Longrightarrow \frac{dh}{dt} = R(t) - f_i(t) \tag{1}$$

where:

$V(t) = A_h h(t)$ is the is the volume of the box (Length^3).

$h(t)$ = water depth (Length).

A_h = surface size of box (Length^2).

The infiltration $f_i(t)$ becomes a function $f_i\left(f_p(t), R(t), h(t)\right)$ as follows:

$$f_i(t) = \left\{ \begin{array}{c} f_p(t) \rightarrow R(t) \geq f_p(t) \\ \dfrac{f_p(t)h(t)}{\max(\eta, h(t))} \rightarrow R(t) < f_p(t) \end{array} \right\} = \Lambda\left(f_p(t), R^k\right)\frac{h(t)f_p(t)}{max\left(\eta, h^k\right)} + \Lambda\left(R(t), f_p(t)\right)f_p(t) \tag{2}$$

here η [Length] is a threshold defining an arbitrary small transition layer and $\Lambda(x,y) = \begin{cases} 1, x > y \\ 0, x \le y \end{cases}$. After substituting Eq. (2) into Eq. (1) we get

$$\frac{dh}{dt} = R(t) - \Lambda\Big(f_p(t), R(t)\Big)\frac{h(t)f_p(t)}{\max(\eta, h(t))} - \Lambda\Big(R(t), f_p(t)\Big)f_p(t) \tag{3}$$

Eq. (3) ensures $h(t) > 0, \forall t$ if and only if $h(0) > 0$, regardless of infiltration or ponding, see in Appendix I.

For small values of η, Eq. (3) is a stiff problem (Lambert, 1999), requiring implicit Euler backward time integration:

$$\begin{aligned} &\frac{h^{k+1} - h^k}{\Delta t} = R^k - f_i^{k+1} \\ &f_i^{k+1} = \left(\Lambda\Big(f_p^k, R^k\Big)\frac{h^{k+1}}{max(\eta, h^\alpha)} + \Lambda\Big(R^k, f_p^k\Big)\right) f_p^k \; h^{k+1} \\ &\rightarrow h_i^{k+1} = \begin{cases} h^k + \Delta t\Big(R^k - f_p^k\Big), R^k \ge f_p^k \\ \dfrac{h^k + \Delta t R^k}{1 + \Delta t f_p^k \big/ max(\eta, h^\alpha)}, R^k < f_p^k \end{cases} \end{aligned} \tag{4}$$

where $h^k \approx h(k\Delta t)$, Δt is the time step and $h^\alpha = (\alpha+1)h^k - \alpha h^{k-1}, 0 \le \alpha \le 1$. Eq. (4) is consistent with Eq. (3). It guarantees positive water depths $\forall \Delta t > 0$ and is inspired by (Patankar, 2018) pp. 145–148 for "always-positive variables".

Fig. 2 shows a numerical experiment with $f_p = 40$ mm/hr and $\eta = 10^{-5}$ mm, a value used throughout this paper. After 20 min of intense rain of 100 mm/hr, it drops to 20 mm/hr, Δt=60 s. Here $\alpha = 1$, for large scale computations we apply $\alpha = 0$.

Fig. 2 shows that the water in the volume box is rising linearly until the rain drops below f_p. During rising and falling of the water depth $f_i = f_p$, until the water depth is below η, then we have $f_i = R$ as can be verified in Fig. 2. Stiff stability of Eq. (4) allows large time steps, while positive values for $h(t)$ and h^k are an intrinsic quality of both Eq. (3) and Eq. (4) without checking h^k. In Section 4, we will implement Eq. (4) in the "**V**olume **C**orrection **E**quation" (VCE) of an SWE-solver.

The formulation described here enables all other sinks, e.g. evaporation, where physical quantities, like volume of water, are required to be always positive. The implicit numerical implementation keeps this important characteristic $\forall \Delta t > 0$. Later in this paper we show that this approach is also used for flooding and drying as a built-in characteristic of the VCE without checking water depths for positivity.

3. Comparison of Horton based models for time dependent infiltration capacity

In Section 2, we introduced SDB with a constant infiltration rate f_p. In this section, we evaluate three Horton type infiltration models with $f_p(t)$ as a function of time. These models include (a) Horton's model (Horton, 1941), (b) SWMM's modification of Horton (Rossman, 2015), and (c) Diskin and Nazimov's model or DNm (Diskin and Nazimov, 1995).

3.1. Horton's infiltration model

This model is given by:

$$f_p(t) = f_c + (f_0 - f_c)e^{-\kappa t} \tag{5}$$

where:

f_p = the actual infiltration capacity [Length/Time].
f_c = the final infiltration capacity [Length/Time].
f_0 = the initial infiltration capacity [Length/Time].
κ = the constant rate of decrease of the infiltration capacity or decay coefficient [1/Time].

These parameters depend on the soil type and are derived from empirical measurements and calibration. Such values are extensively documented in the literature, e.g. (Rossman, 2015).

3.2. SWMM's modified Horton's infiltration model

This model is given by:

$$f_p(t) = f_c + (f_0 - f_c)e^{-\kappa t_p} \tag{6}$$

t_p is defined by Eq. (7). Horton's infiltration formula is valid only where the actual infiltration is always

equal to the infiltration capacity. In case of thin water layers at the surface and rain less than f_p, Eq. (5) is not valid. To adjust this, a pseudo

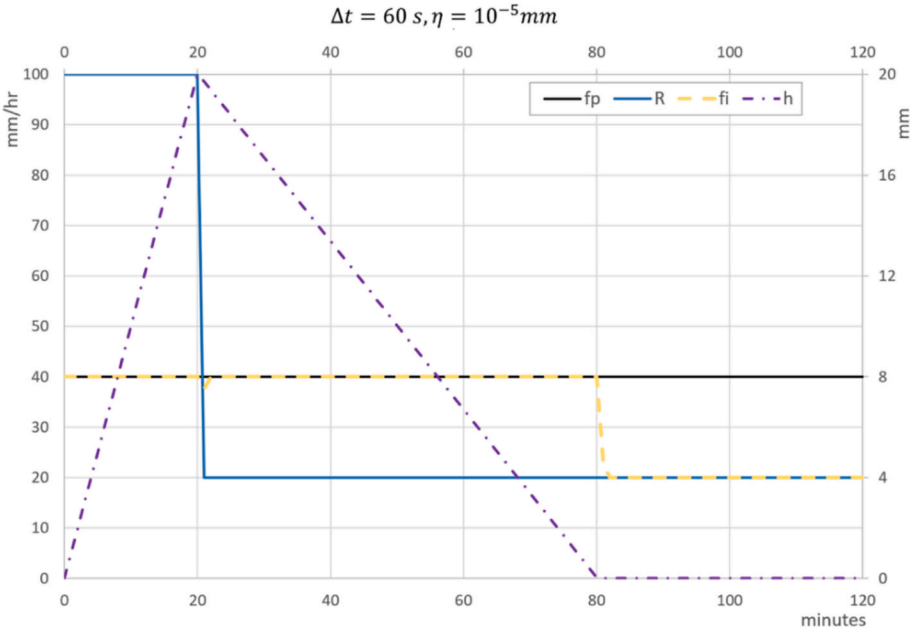

Fig. 2. Computations of infiltration capacity f_p, infiltration f_i and ponding water depth h as response to rainfall R for SDB in the Volume Box Experiment; time step used is 1 min.

time t_p is introduced as follows:

$$\int_0^{t_p} f_p(t)dt = f_c t_p + \frac{f_0 - f_c}{\kappa}(1 - e^{-\kappa t_p}) = \int_0^t f_i(t)dt \tag{7}$$

where $\int_0^{t_p} f_p(t)dt$ equals the cumulative infiltration calculated as $\int_0^t f_i(t)dt$

For explicit values of t_p a solution is obtained by iterations (Viessman and Lewis, 2003). In SWMM (Rossman, 2015) this model also contains a function for recovery of the infiltration capacity once infiltration has stopped. The equation used is:

$$f_r(t) = f_0 + (f_c - f_0)e^{-\kappa_d(t - t_w)} \tag{8}$$

with

κ_d = recovery rate,.$\kappa_d \ll \kappa$

f_r = infiltration capacity during recovery.

t_w = time factor to ensure continuity of f_p and f_r at the transition from f_p to f_r.

3.3. Diskin and Nazimov's infiltration model

DNm consists of 2 components: A regulating element and a storage box. We have replaced the regulating element by our SDB, getting the boxes B1 and B2, see Fig. 3.

B1 is the SDB described in Section 2. For B2 the following equation are applied:

$$\frac{dz}{dt} = f_i(t) - f_g(t) \tag{9}$$

$$f_g(t) = f_c z(t) \Big/ z_{max} \tag{10}$$

$$f_p(t) = f_c + (1 - z(t)/z_{max})(f_0 - f_c) \tag{11}$$

where:

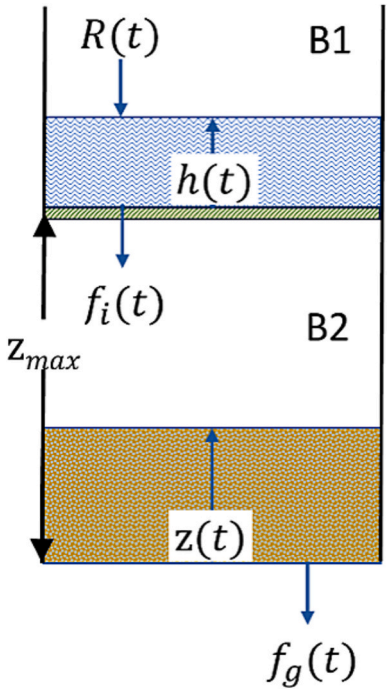

Fig. 3. Extension of SDB with a storage box for Diskin and Nazimov model (DNm).

z_{max} = maximum height of B2.

$z(t)$ = water depth in B2, also viewed as moisture content .$z(t)/z_{max}$

$f_g(t)$ = outflow from B2.

DNm is equivalent to Horton's model if $R(t) > f_p(t) \forall t$ and $z_{max} = f_0/\kappa$. DNm can be viewed as a mathematically robust formulation of the concepts to improve Horton's model with respect to recovery of infiltration capacity. Our SDB formulation generalises the DNm further to incorporate seamlessly change in infiltration capacity due to spatio-temporally varying rainfall intensity and ponding water depths. For detailed analysis see the Appendix II and (Diskin and Nazimov, 1996).

3.4. Numerical implementation of the double box model

The overall numerical scheme consists of two consecutive implicit integration steps for B1. The first step is given by Eq. (4). The second step, with f_i^{k+1} taken from Eq. (4), reads:

$$\frac{z^{k+1} - z^k}{\Delta t} + \frac{f_c}{z_{max}} z^{k+1} = f_i^{k+1} \tag{12}$$

Eq. (11) can be written as:

$$f_p^{k+1} = f_c + (1 - z^{k+1}/z_{max})(f_0 - f_c) \tag{13}$$

3.5. Comparison of Horton, SWMM and DNm

To illustrate the difference between the three models we conduct 3 numerical experiments: Experiment 3.I is a simplified experiment, without any rain, resembling an infiltrometer (Karahan and Pachepsky, 2022; Viessman and Lewis, 2003). The water depth is maintained at a constant level $h > \eta$ such that the infiltration is always equal to the infiltration capacity. Experiment 3.II explores the difference in decay of infiltration capacity for a precipitation curve that is both below and above the infiltration capacity. 3.III has two rain peaks within 3 days. Both ponding and the development of infiltration capacity is compared.

3.5.1. Experiment 3.I

All the models are equivalent in computing infiltration capacities when water level is kept constant without rainfall. See Fig. 4.

3.5.2. Experiment 3.II

This experiment evaluates computed decay and recovery of infiltration capacity including ponding for the following parameters $f_0 = 25cm/hr$, $f_c = 2.5cm/hr$, $1/\kappa = 2hrs$. Results are shown in Fig. 5. The rain is:

$$t \le 6T_h, R(t) = .5f_0 \exp((t - 3T_h)/T_h)^2,\ T_h = 3600\,s,\ t > 6T_h, R(t) = 0$$

Fig. 5 shows considerable difference between Horton's model and SWMM. Infiltration based on the original Horton model only depends on time, a well-known drawback. The differences between SWMM and DNm are minor, except DNm does not require non-linear iterations and transition checks from decay to recovery or vice versa.

3.5.3. Experiment 3.III

For this experiment we only compare SWMM and DNm. The differences concern $f_p(t)$ during low rainfall, $R(t) < f_c$, where the SWMM recovery of f_p is conceptually different from DNm.

For SWMM, f_p will switch from Eq. (6) to Eq. (8) in case of zero infiltration. For Eq. (8) we get $\lim_{t\to\infty} f_r(t) = f_0$. For DNm a switch is not required. Recovery is a built-in characteristic. The recovery limit is given by:

$$\lim_{t\to\infty} f_p(t) = (1 - R/f_c)f_0 + R \tag{14}$$

See Appendix II for more details.

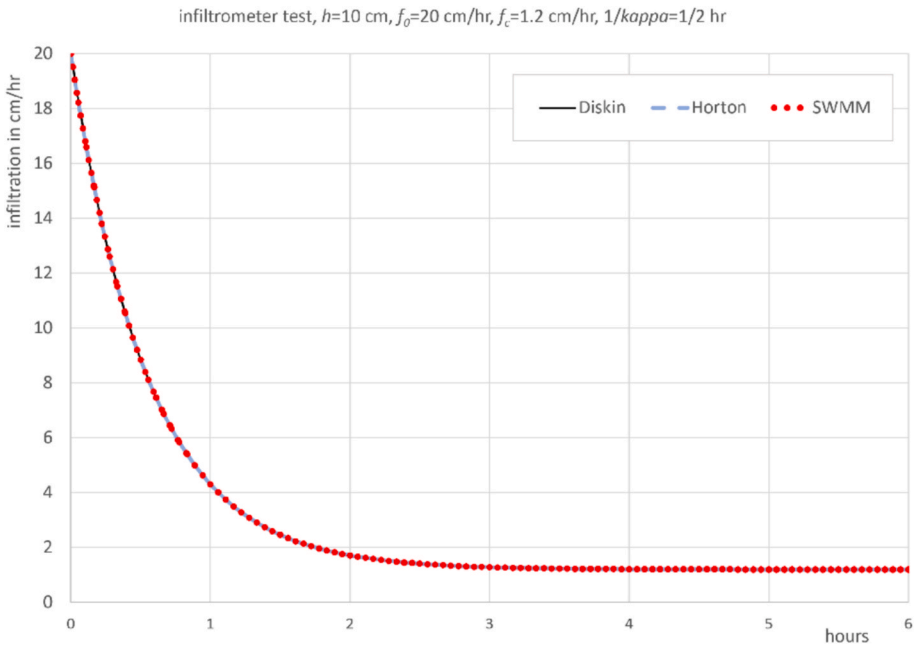

Fig. 4. Experiment 3.I, Infiltrometer simulation, all Horton models show the same decay of infiltration capacity.

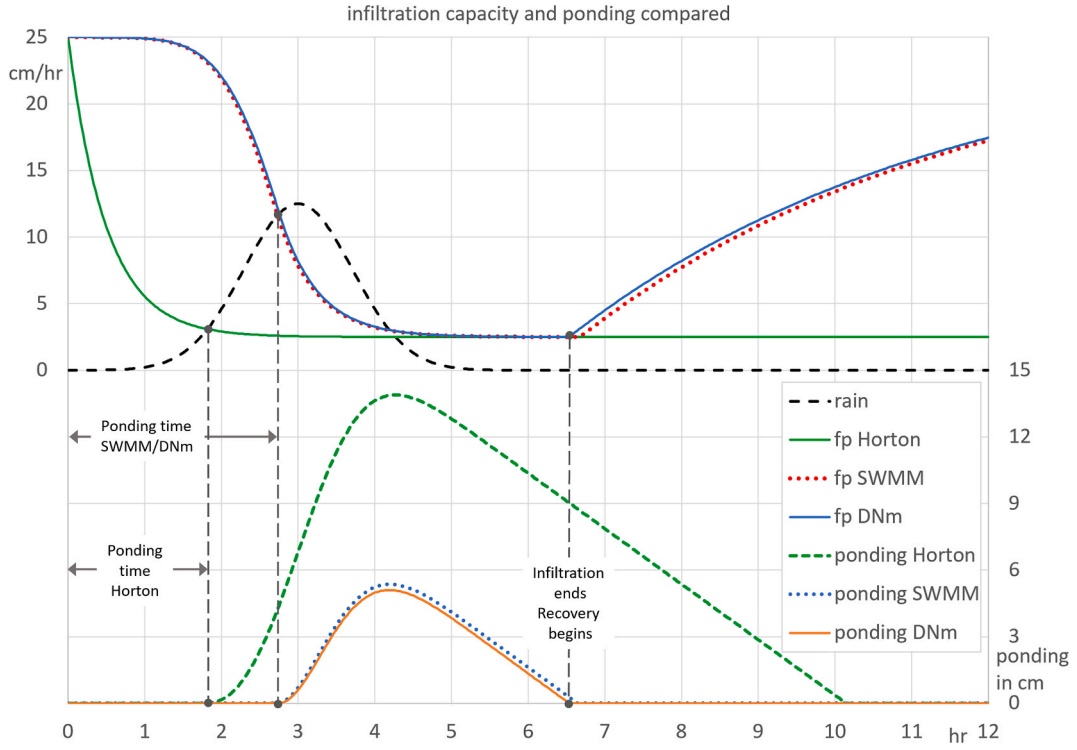

Fig. 5. Experiment 3.II, Infiltration capacity and ponding compared for 3 different Horton models, basic Horton has no recovery.

To illustrate the differences, Experiment 3.III has intermittent rain peaks, based on Gaussian functions shifted in time but equal to Experiment 3.II, see Fig. 6. We have two rain peaks as follows:

$$R_1(t) = .5f_0\exp((t-15T_h)/T_h)^2$$
$$R_2(t) = .5f_0\exp((t-39T_h)/T_h)^2$$
$$T_h = 3600\,\mathrm{s}$$

For the following intervals:

$$0 \le t < 15T_h, R(t) = \max(.5f_c, R_1(t))$$
$$15T_h < t < 18T_h, R(t) = R_1(t)$$

$$18T_h \le t \le 36T_h, R(t) = 0$$

$$36T_h < t \le 39T_h, R(t) = R_2(t)$$
$$39T_h < t \le 72T_h, R(t) = \max(.5f_c, R_2(t))$$

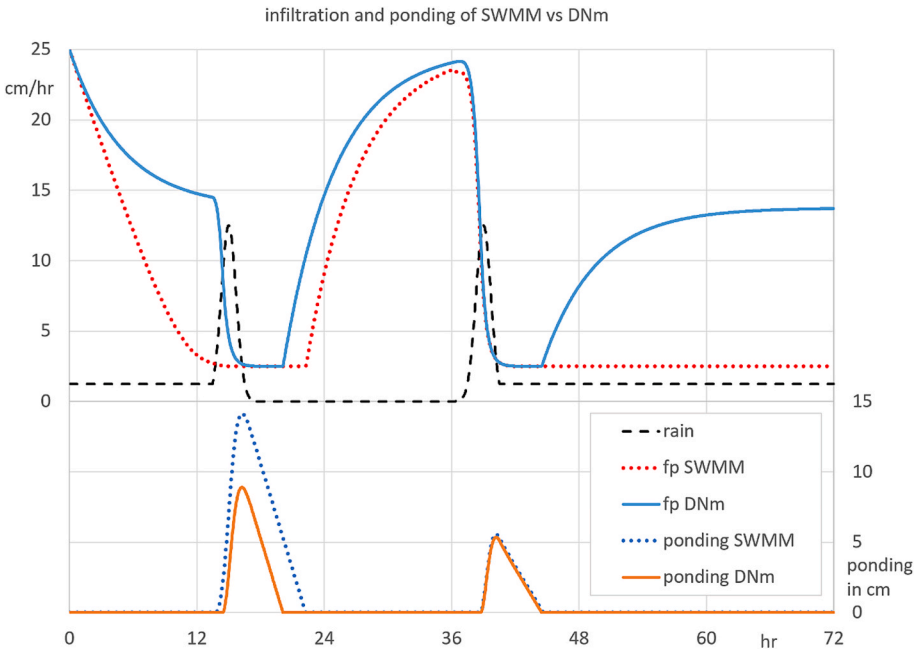

Fig. 6. Experiment 3.III, Infiltration capacity and ponding compared for 2 different modified Horton models with an intermittent rain curve.

We have chosen a recovery rate $\kappa_d = \frac{f_c}{f_0}\kappa$. In the first section both models tend to their limiting values. For $0 < R < f_c$ SWMM has the same limit f_c, but takes longer to get there. For $R = 0, f_p = f_0$. This is an unrealistic discontinuity in contrast to DNm. During the peak rainfall both models show ponding. The largest ponding is by SWMM, since it starts at almost its minimum infiltration capacity. During the dry interval both models recover to almost the same infiltration capacity. SWMM starts recovering a little later, since more ponded water must be infiltrated before recovery starts. During the second peak the models behave almost equally, like in Fig. 5. Since the infiltration capacities are equal, ponding is also equal, see Fig. 6. After the second peak, there is no recovery for SWMM and partial recovery for DNM. However, infiltration capacity depends on the soil moisture content of soils surface layer. If $f_i < f_c$ then the soil moisture content, $z(t)/z_{max}$, will decrease and $f_p(t)$ will increase. Conceptually, this is more realistic than recovery only during zero infiltration.

For implementation in SWE, DNm is the best option among the compared methods, due to its simplicity without non-linear equations and switches between decay and recovery or vice versa, and its conceptually better recovery of $f_p(t)$. Moreover, with additional parameters, Eq. (10) can be modified to change its outcome. For example, (Shao and Baumgartl, 2016) presents an algorithm for a modified Horton model that is essentially a numerical approximation of this paper's Eq. (9) and Eq. (10). The difference is the time integration. We use implicit Euler (Lambert, 1999), for robustness in large scale 2D applications, while (Shao and Baumgartl, 2016) employs explicit Euler. In (Shao and Baumgartl, 2016), there is also an algorithm for an "improved modified Horton model" that is in essence an adjustment of the Eq. (10). Essentially, Eqs. (9)–(11) can be interpreted as a generalised form of modified Horton's infiltration, where other modified Horton's formulations can be considered special cases of this formulation. This means that we consider DNm a versatile starting point for implementation in sub-grid 2D SWE solvers, with options for future adjustments.

4. SWE for rainfall-runoff with DNm

We use SWE in this section since for real-world runoff problems in domains which have areas where simplifications of SWE, such as kinematic wave equations or diffusive wave equations (Chanson, 2004), cannot be applied. Examples are: ponds of deep water, rivers or intertidal zones surrounding the area of interest.

4.1. Numerical approximations

The 2D SWE are given by momentum equations in x- and y directions and the continuity equation:

$$\begin{aligned} u_t + uu_x + vu_y + g\zeta_x + \frac{c_f}{h}u\|u\| = 0 \\ v_t + uv_x + vv_y + g\zeta_y + \frac{c_f}{h}v\|u\| = 0 \end{aligned} \tag{15}$$

$$h_t + (uh)_x + (vh)_y = R(x,y,t) - f_i\left(R, f_p, h, \eta\right) \tag{16}$$

where:

$u, v(x,y,t)$ = depth-averaged velocities in x and y direction
g = gravity.
$\zeta(x,y,t)$ = water level above the reference plane.
c_f = dimensionless bed friction coefficient e.g. $c_f = g/(C_z)^2$,
C_z= Chezy coefficient, C_z is constant or .$C_z = h^{1/6}/n$
n = Manning coefficient.
$e(x,y)$ = bed level above plane of reference .
$h(x,y,t)$ = water depth,.$h(x,y,t) = \zeta(x,y,t) - e(x,y)$
$f_i\left(R, f_p, h, \eta\right)$ = infiltration based on DNm and Eq. (2), parameters varying with .x,y,t
$R(x,y,t)$ = spatiotemporal rainfall.

The numerical approximation is based on clustering high resolution sub-grids (Stelling, 2012), see Fig. 7. The sub-grid method is highly efficient for large scale flooding simulations based on DTMs, as described in (Kennedy et al., 2019; Ruheili et al., 2019; Wang et al., 2014; Hsu et al., 2016). Like any method it has drawbacks requiring improvement (Casulli, 2019; Hodges, 2015; Stelling,. 2022). Optimal bed friction treatment for sub-grids is described in (Van Ormondt et al., 2025; Volp et al., 2013). Well-known flood simulators such as HEC-RAS (Army Corps, 2025) and TUFLOW (WBM Pty Ltd, 2025) based on SWE solutions have incorporated the sub-grid technique (Artiglieri et al., 2025).

The SWE are discretized by a conservative Finite Volume Method

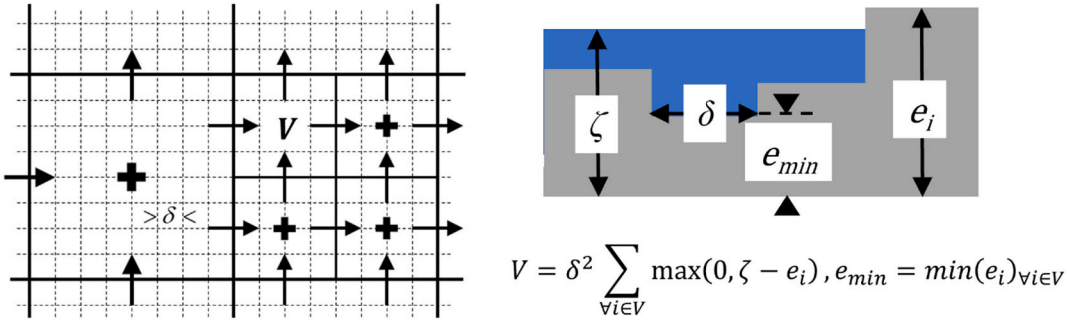

Fig. 7. Top view and side view of a staggered quadtree grid with DTM as sub-grid.

(FVM). The grid is a quadtree (Stelling, 2012), with clustered DTM pixels as sub-grid, see Fig. 7. The variable grid size Δx_l is always an even multiple of the pixel size δ of the DTM. The continuity equation is mildly non-linear, or piecewise linear (Casulli, 2009). Conservation requires Newton iteration (Brugnano and Casulli,. 2008), but we compute only the first step of this procedure as a predictor, without iteration. Conservation, flooding and drying are an intrinsic part of the corrector (Stelling,. 2022). For the semi-implicit time integration, the θ-method is applied with explicit wet cross sections as predictor. Momentum advection may be locally implicit, utilizing Carlson's method (Kramer and Stelling, 2008; Stelling, 2012). The resulting numerical approximations are:

$$\left.\begin{aligned} \frac{u^{k+1}-u'}{\Delta t} + gD_x\zeta^* + c_f^k\frac{u^{k+1}\|u^k\|}{h^k} = 0 \\ \frac{v^{k+1}-v'}{\Delta t} + gD_y\zeta^* + c_f^k\frac{v^{k+1}\|u^k\|}{h^k} = 0 \end{aligned}\right\} \tag{17}$$

Predictor step, for the non-conservative continuity equation for volume V, not integrated with SDB:

$$S_V^k\frac{(\zeta_V^* - \zeta_V^k)}{\Delta t} - \sum_{\forall u_I^k \in V} A_I^k u_I^{k+\theta} + \sum_{\forall u_o^k \in V} A_o^k u_o^{k+\theta} = S_{max_V}\left(R_V^k - min\left(\frac{V^k}{\Delta t S_{max_V}} + R_V^k, f_{p_V}^k\right)\right) \tag{18}$$

Conservative Volume Correction Equation, VCE, integrated with SDB:

$$Q_{i_V}^* = S_{max_V} f_{p_V}^k$$

if $Q_{R_V}^k \geq Q_{i_V}^*$ *then* :

$$\frac{V^{k+1}-V^k}{\Delta t} + \frac{V^{k+1}}{V^k}\sum_{\forall Q_O^* \in V} Q_O^* = \sum_{\forall Q_+^* \in V}\frac{V_I^{k+1}}{V_I^k}Q_I^* + Q_{R_V}^k - Q_{i_V}^* \tag{19}$$

else if $Q_{R_V}^k < Q_{i_V}^*$ *then* :

$$\frac{V^{k+1}-V^k}{\Delta t} + \frac{V^{k+1}}{V^k}\left(\sum_{\forall Q_O^* \in V} Q_O^* + Q_{i_V}^*\right) = \sum_{\forall Q_+^* \in V}\frac{V_I^{k+1}}{V_I^k}Q_I^* + Q_{R_V}^k$$

$$V\left(\zeta_V^{k+1}\right) = V^{k+1} \tag{20}$$

The final step of DNm for every volume V we have:

$$\frac{z_V^{k+1}-z_V^k}{\Delta t} + f_{c_V}\frac{z_V^{k+1}}{z_{max_V}} = f_{i_V}^{k+1}$$

$$f_{i_V}^{k+1} = \begin{cases} f_{p_V}^k, R_V^k \geq f_{p_V}^k \\ \dfrac{V^{k+1}}{max\left(\eta S_{max_V}, V^k\right)} f_{p_V}^k, R_V^k < f_{p_V}^k \end{cases} \tag{21}$$

$$f_{p_V}^{k+1} = f_{c_V} + \left(1 - \frac{z_V^{k+1}}{z_{max_V}}\right)\left(f_{0_V} - f_{c_V}\right) \tag{22}$$

where:

$D_{x,y}\zeta$ = numerical surface gradients.
c_f^k = dimensionless bed friction
A = wet cross section facing volume V.
u_I = input velocity to volume V that is normal to its face .A_I
u_O = output velocity of volume V that is normal to its face .A_O
$Q_I^* = A_I^k u_I^{k+\theta}$
$Q_O^* = A_O^k u_O^{k+\theta}$

θ = weighting factor for implicitness.
$u^{k+\theta} = (1-\theta)u^k + \theta u^{k+1}$
$adv(u, v)$ = advection approximations.
$u' = u^k + \Delta t\left(\beta adv\left(u^k\right) + (1-\beta)adv(u')\right), \beta = \min\left(1, \frac{1}{C_u}\right)$, see (Kramer and Stelling, 2008; Stelling and Duinmeijer, 2003; Stelling, 2012).
$v' = v^k + \Delta t\left(\beta adv\left(v^k\right) + (1-\beta)adv(v')\right)$ see u'
C_u = velocity Courant number.
ζ_V^{k+1} = water level in volume $V(\zeta_V^{k+1})$
$V\left(\zeta_V^{k,k+1}\right)$ = piecewise linear volume function (for V at V we omit the index V).
V_I = volume taken from the up-winded/input direction of u_I at cross section A_I
$V_O = V$, volume taken from the out direction of u_O at cross section A_O is always equal to V
$Q_{R_V} = S_{max_V} R_V$
$Q_{i_V} = S_{max_V} f_{i_V}$
$f_{i_V}^{k+1}$ = actual infiltration
$\left(f_{i_V}^{k+1} = \Lambda\left(f_{p_V}^k, R_V^k\right)\frac{V^{k+1}}{max\left(\eta S_{max_V} V^k\right)} f_{p_V}^k + \Lambda\left(R_V^k, f_{p_V}^k\right) f_{p_V}^k\right)$
$e_{V,min}$ = the lowest pixel of V.

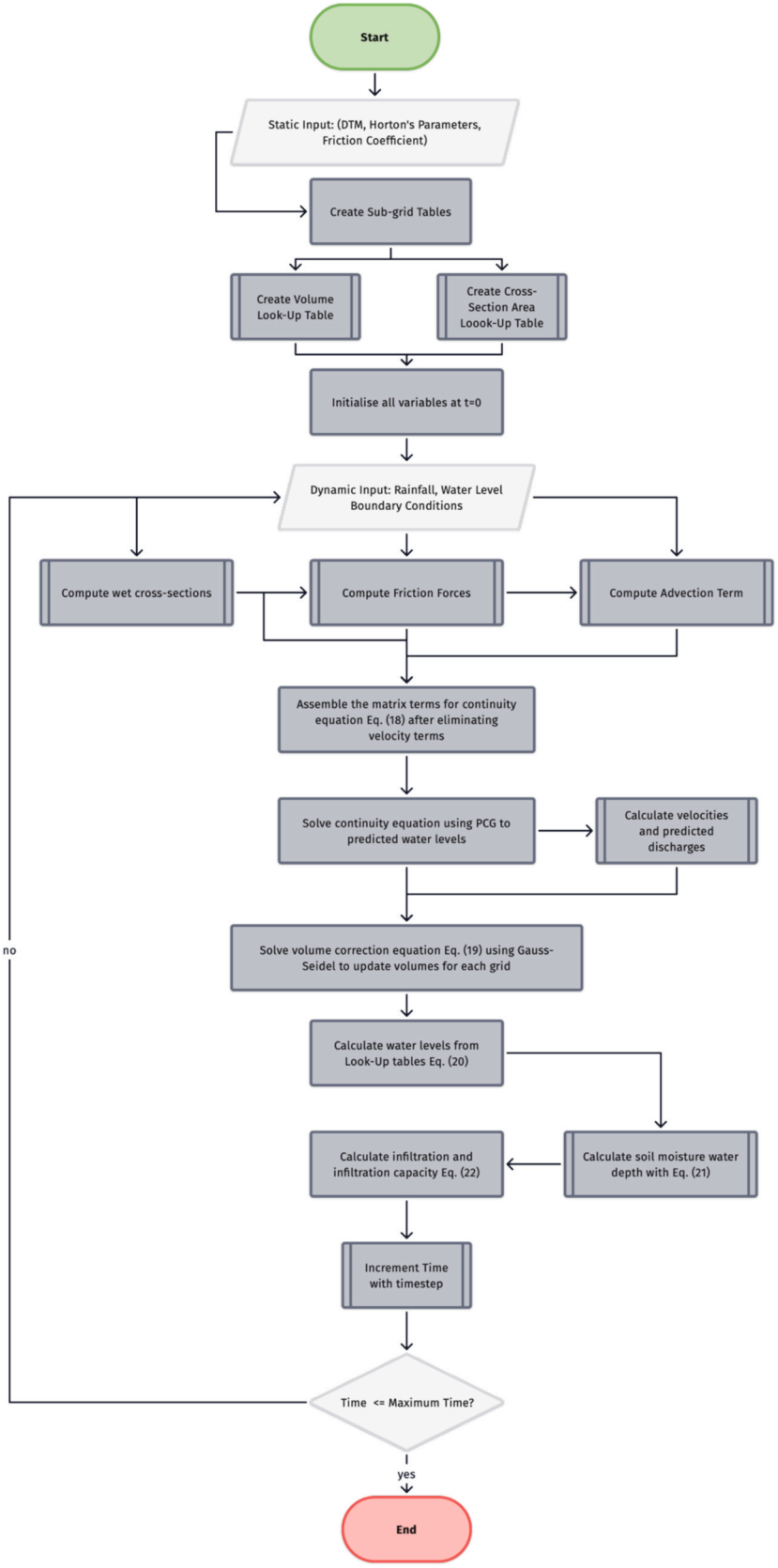

Fig. 8. Flowchart describing the time integration of the 2D DNm-SWE solver.

R_V^k = precipitation

$S_V(\zeta_V^k)$ = surface of all wet pixels of volume V with water level ζ_V^k.

S_{max_V} = maximum surface of a grid cell with all pixels wet$(S_{max_V} = \sum_{\forall \delta \in V} \delta^2)$

f_{c_V} = the minimum infiltration capacity of volume V.

$f_{p_V}^k$ = infiltration capacity of volume V.

f_{0_V} = the maximum infiltration capacity of volume V.

z_V = water depth/moisture content (z_V / z_{max_V}) of box connected with V.

z_{max_V} = maximum height of storage box connected with volume V.

$?^*$ = all symbols marked with an asterisk are predicted values that will be corrected.

After elimination of u^{k+1} from Eq. (18), by substitution of Eq. (17) into Eq. (18), Eq. (18) is solved by a preconditioned Conjugate Gradient method (Golub and Van Loan, 2013). Eq. (19) is strictly conservative and is linear, solved very efficiently by Gauss Seidel's method (Stelling, 2022; Varga, 2000). Eq. (19) yields implicit correction factors V^{k+1}/V^k for the cross sections $A_{I,O}^k$, ensuring $V^{k+1} > 0$ and $h_V^{k+1} = \zeta_V^{k+1} - e_{V,min} > 0, \forall \Delta t > 0$. Eq. (20) defines the value of ζ_V^{k+1}. V is a table function (Stelling, 2012), that determines ζ_V^{k+1} by a local linear equation. Smooth flooding and drying are guaranteed $\forall \Delta t > 0$ without checking cells for drying. The method is robust and suitable for different flow conditions, including rapidly varied flows (Kramer and Stelling, 2008; Stelling and Duinmeijer, 2003). The time integration with DNm-SWE sub-grid solver is summarised in Fig. 8. Appendix III shows, step-by-step, an implementation of the Eqs. (17)–(22) for 3 volumes.

4.2. 2D Real-World example

The DNm-SWE model is applied to a catchment in New South Wales, Australia to assess its computational ability with different rainfall forcing on heterogenous surface conditions to validate its applicability for real-world use. The Upper Parramatta River catchment (Fig. 9) is approximately 110 square kilometres and located upstream of Sydney between 150° 54.25′ E and 151° 3.41′ E longitudes and 33° 50.70′ S and 33° 43.71′ S. It contains the watershed for the river Parramatta that flows into Sydney Harbor. The city of Parramatta lies within the catchment. The catchment faces flood risk due to rainfall, since rainfall often exceeds 200 mm in 72 h (Parramatta and Sydney, 2024) and therefore has an operational flood warning system in this catchment maintained by the City of Parramatta Council (Flood Warning Service | City of Parramatta, 2024). The area is densely urbanized near the river but also contains vegetated areas.

4.2.1. Model data and setup

The DTM for the Upper Parramatta River Catchment is from the Geoscience Australia (Geoscience Australia Portal, 2024) at a resolution of $1 \times 1m^2$. The altitudes vary between 191 m and −9 m Australian Height Datum (AHD), see Fig. 9. The terrain profile near the riverbanks is flat with a slope less than 1 % but is surrounded by hilly terrain and creeks where some slopes are steeper with 3 % in some areas. The catchment outlet point in this model is just south of the Charles Street Weir, outside the intertidal zone. This makes the model convenient for rainfall-runoff simulation as the flooding is purely driven by rainfall-runoff.

Rainfall intensities every 5 min are obtained from the Bureau of Meteorology Australia (Water Data Online: Water Information: Bureau of Meteorology, 2024) from six stations in and around the Upper Parramatta River catchment (Fig. 9). Water level observations at three stations along the Parramatta River are available from the WaterNSW portal (WaterInsights - WaterNSW, 2024). The gauge locations are shown in Fig. 8.

Land use data is available on the Geoscience Australia portal (Portal, 2024) from a couple of sources– (a) the Digital Earth Australia Landcover layer which is derived from the Landsat satellite observations at 30 m resolution and (b) Catchment Scale Land Use 2020. Based on these datasets, the primary land use categories in the catchment are dense urban (~17 %), mixed urban including urban bushlands and parks (~58

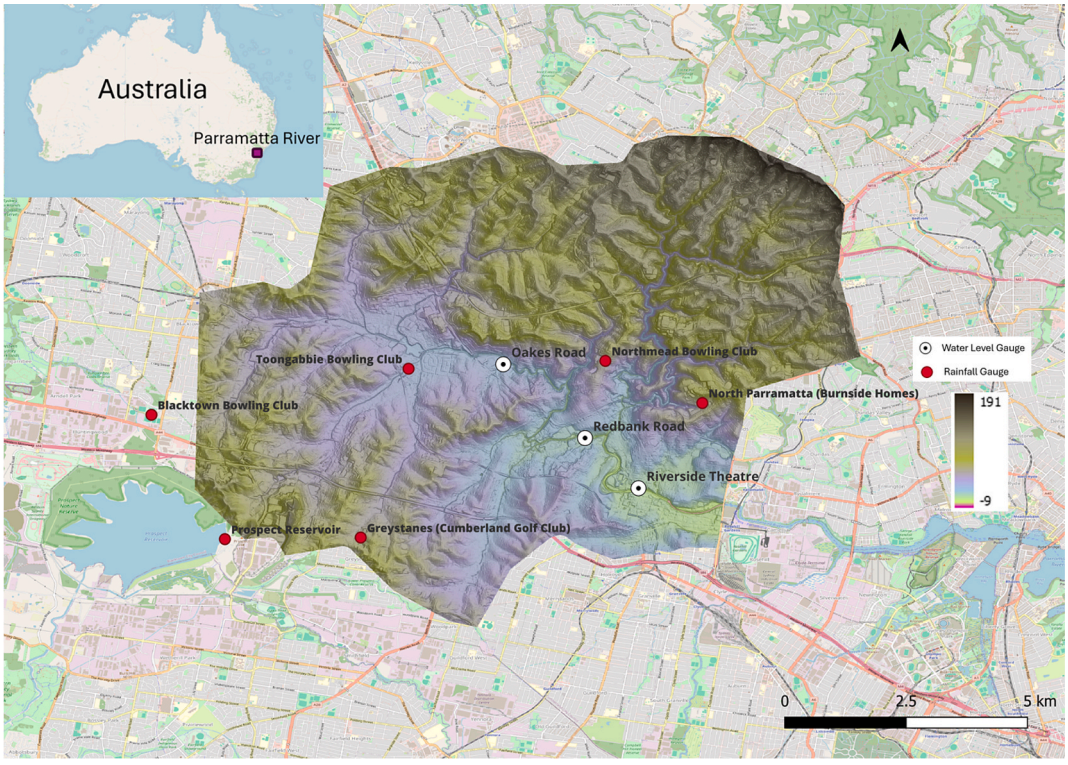

Fig. 9. Digital Terrain Model (DTM), Water Level Gauges and Rainfall Gauges for the Upper Parramatta River Catchment model domain and the location of Parramatta River in New South Wales Australia overlaid on OpenStreetMap©.

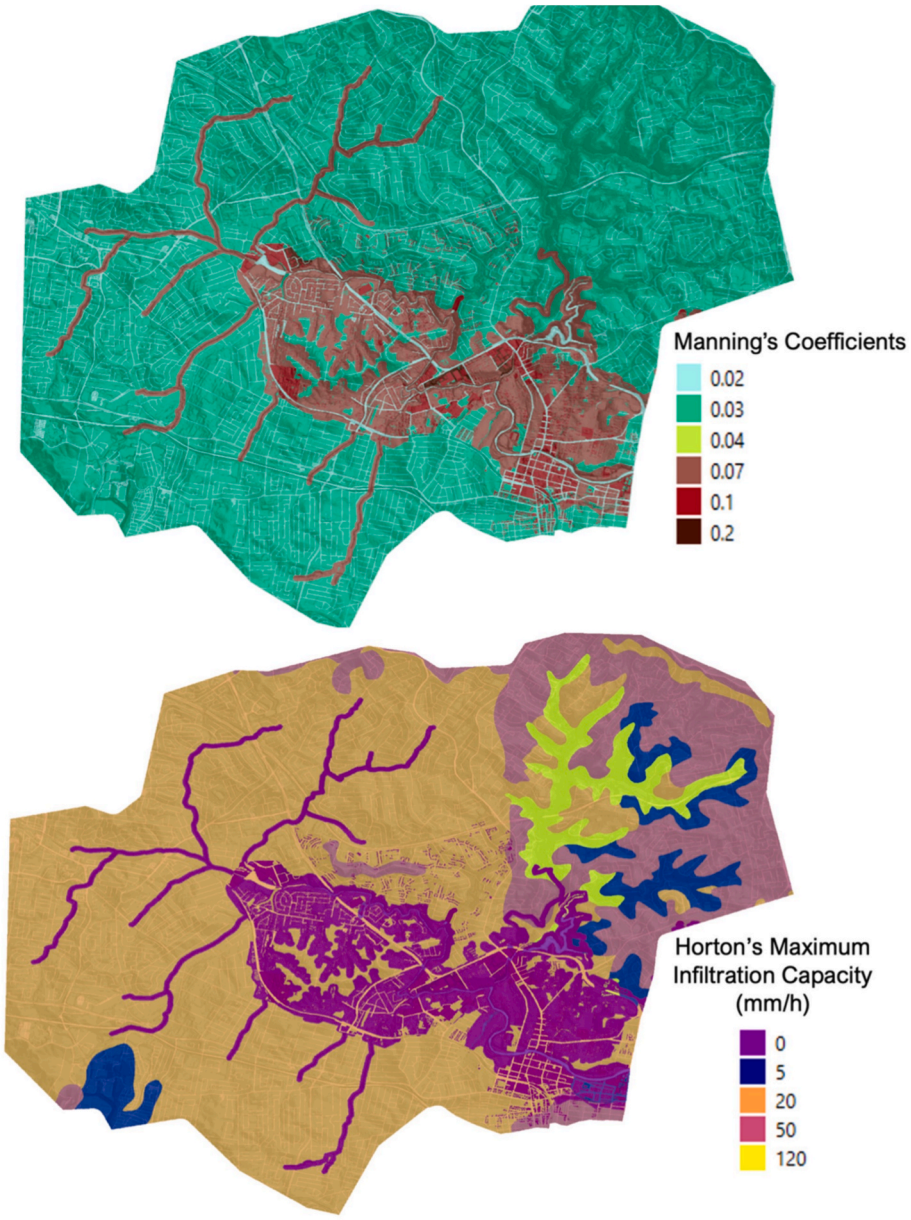

Fig. 10. Spatial Distribution of (a) Manning's Roughness Coefficients [top] and (b) Horton's infiltration model parameters [bottom] across the model domain used in the computational model setup.

Table 1
Infiltration parameters for DNm applied in the computational model setup for Upper Parramatta.

Class	Maximum Infiltration Capacity (mm/hr)	Minimum Infiltration Capacity (mm/hr)	Decay coefficient (1/hr)	Percentage area of model domain
a	120.0	6.5	3	4.05 %
b	50.0	2.5	3	15.70 %
c	20.0	1.0	3	58.70 %
d	5.0	1.0	3	4.96 %
e	0	0	0	18 %

%), forest, reserved parks and wetlands (~19 %), natural water courses (~2%), transportation network (~1%) and bare ground (~1%). These land cover categories are used to define the Manning's friction coefficients between 0.02 and 0.2 across the domain (Fig. 10a).

Soil type data is obtained from the NSW Soil and Land Information Portal (Australian Soil Classification, 2024) which contains the different soil type contours according to the Australian Soil Classes (ASC). Another source of information about the soil groups is from the Global Hydrologic Soil Group dataset at 250 m resolution (Ross et al., 2018). According to these datasets, some areas have Calcerous sand and Alluvial Light sand (~4%) and Heavy Alluvial Soil (~15 %). Majority of the area has Brown Podzolic Soils (~60 %) and the remaining areas have Alpine Humus Soil, Solodic Soil, Soloth soils. In terms of Hydrologic Soil Groups (HSG) classes the catchment mainly has HSG-C/D and HSG-D/D soil types, and some HSG-C and HSG-D type of soil – which indicates less than 50 % sand everywhere. These soil types are overlaid with the land use information to create 5 classes of Horton's parameters in the model (see Table 1). They are categorized as sandy with forest and other vegetation (class 'a'), alluvial soil with mixed land use (class 'b'), clayey or loamy soil with mixed land use (class 'c'), clayey soil with high runoff potential (class 'd') and impervious zones (class 'e'). The spatial distribution of these classes is shown in Fig. 10b. The parameters used for this model represent realistic heterogeneity of the surface to demonstrate,

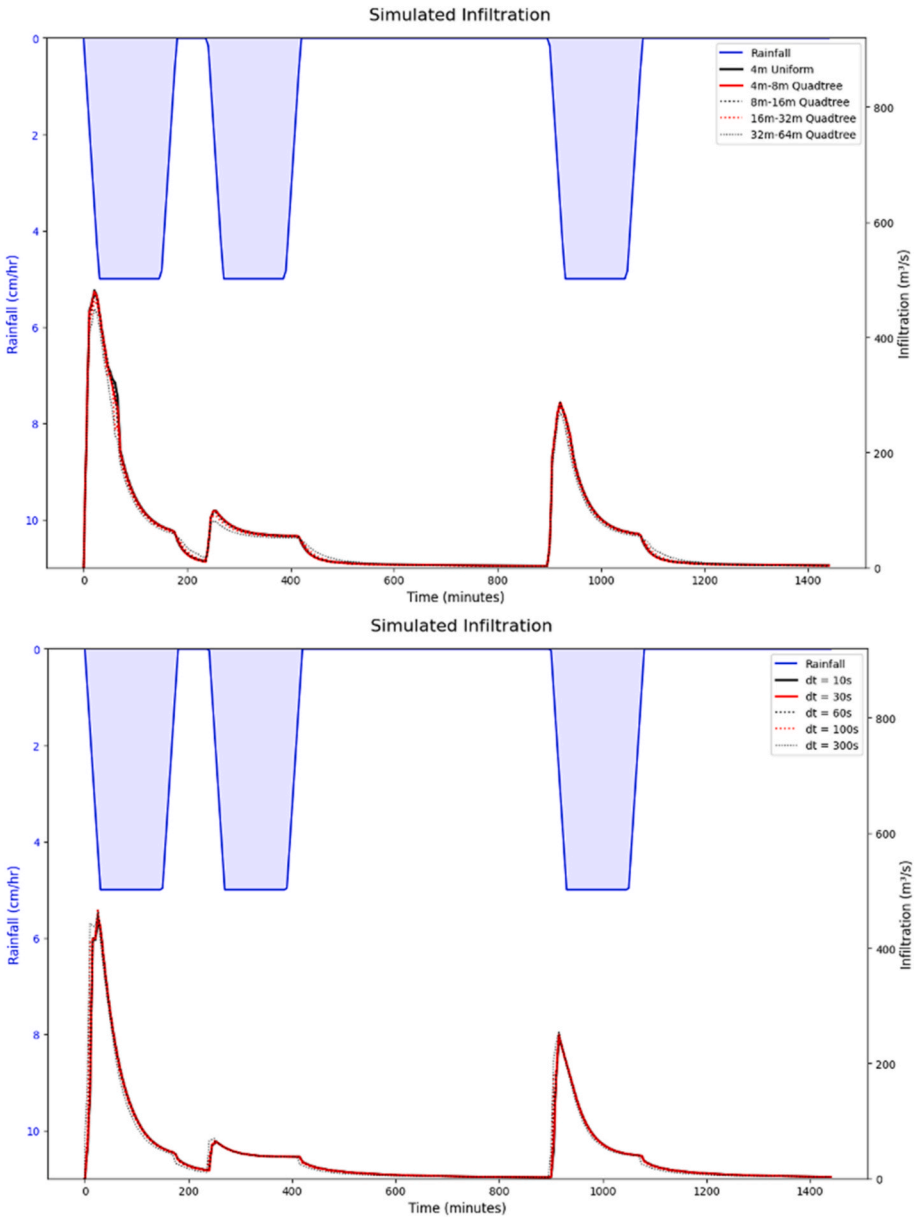

Fig. 11. Sensitivity of computed infiltration to (a) computational grid size [top] and (b) computational time step [bottom].

without calibration, the capability of our DNm-SWE.

4.2.2. Synthetic event

Here we apply synthetic intermittent rainfall during 24 h over the entire catchment. The rainfall curve has 3 peaks of 50 mm/hr, each peak sustained for 2 h. For each rain event the rainfall intensity increases from 0 mm/hr to 50 mm/hr in 30 min and decrease from 50 mm/hr to 0 mm/hr in 30 min.

To demonstrate the recovery of infiltration capacity during periods of no rainfall, the first dry period between the first and second rainfall peaks is 2 h and the second dry period between second and third rainfall peak is 9 h. To test the effect of computational grid sizes on runoff and infiltration and find appropriate balance between accuracy and computational speed, quadtree grids with two levels are applied, where a refinement is used in the flood plain zone of the Parramatta River.

The DNm-SWE model has been implemented in Fortran incorporating OpenMP directives to enable multi-core shared memory parallel execution and was compiled with the Intel Fortran Compiler v2020.9. The simulations for Upper Parramatta River Catchment case were performed on an AMD Ryzen Threadripper PRO 5995WX CPU with 64 cores.

Simulations of different models, varying by grid size and timestep were conducted to evaluate the sensitivity of runoff and infiltration rate. Infiltration calculations are stable for different computational grids (Fig. 11a) and for timesteps ranging from 10 s to 300 s (Fig. 11b). The total infiltration $\sum f_i$ is also stable for each timestep across the model domain, indicating the robustness of the SDB formulation for DNm.

The hydrographs show slight variations in terms of the phase and the peaks, see Fig. 12a. This is particularly the case for the rising limbs of the hydrographs, especially visible when the 4 m uniform grid results are compared to the other quadtree grid configuration results. The finest grid results in delays of $\pm$ 30 min in the runoff peaks compared to the quadtree grids. Hence, it is recommended to determine a suitable computational grid resolution that offers a balance between accuracy and computational efficiency based on a convergence test. In this case, it seems that the quadtree, with an 8 m fine grid and 16 m coarse grid, offers that optimum, see Table 2. The computational time can vary between 2 h and 15 min to 13 s without affecting volume conservation.

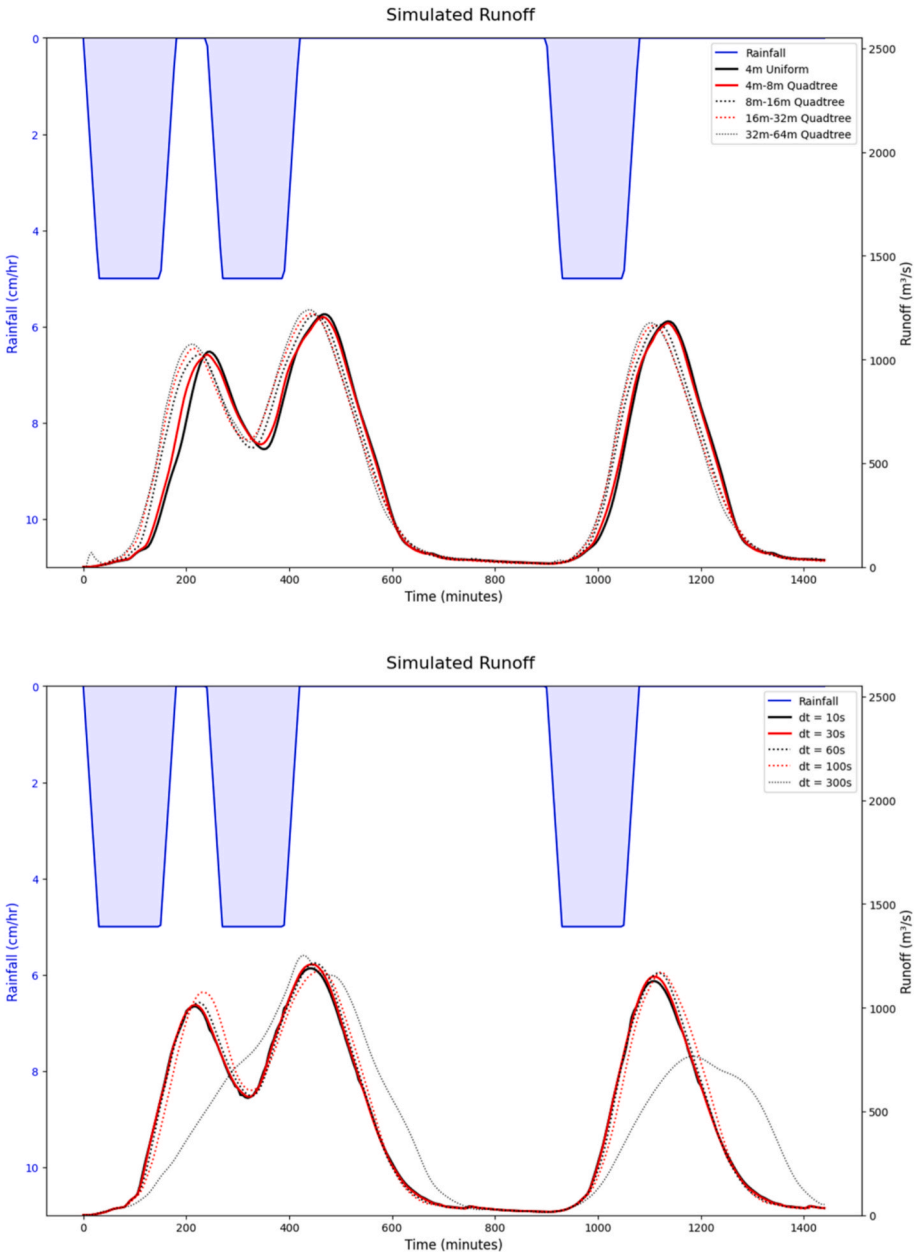

Fig. 12. Sensitivity of runoff computations to (a) computational grid size [top] and (b) computational time step [bottom].

Table 2
Summary of simulations with different computational grids and timesteps in terms of volume error and computational time.

Grid Type	Grid Size	Time step	Total number of timesteps	Computational Grid Points	Computational Time	Volume Balance Error (m^3)
Uniform	4 m x 4 m	60 s	1440	7,155,445	2 h and 15 min	1.4×10^{-5}
Quadtree	4 m x 4 m and 8 m x 8 m	60 s	1440	2,413,036	20 min and 31 s	5.6×10^{-5}
Quadtree	16 m x 16 m and 32 m x 32 m	60 s	1440	152,637	46 s	6.9×10^{-7}
Quadtree	32 m x 32 m and 64 m x 64 m	60 s	1440	38,773	13 s	1.1×10^{-6}
Quadtree	8 m x 8 m and 16 m x 16 m	60 s	1440	606,102	3 min and 42 s	2.1×10^{-5}
Quadtree	8 m x 8 m and 16 m x 16 m	10 s	8640	606,102	12 min and 31 s	2.1×10^{-5}
Quadtree	8 m x 8 m and 16 m x 16 m	30 s	2880	606,102	5 min and 24 s	2.0×10^{-5}
Quadtree	8 m x 8 m and 16 m x 16 m	100 s	864	606,102	2 min and 35 s	2.1×10^{-5}
Quadtree	8 m x 8 m and 16 m x 16 m	300 s	288	606,102	2 min and 29 s	2.2×10^{-5}

This is owed to the sub-grid method combined with the volume correction equation in Eq. (19). The computational speeds demonstrate the efficiency of the predictor–corrector approach over Newton type iterations for non-linear solutions resulting from sub-grid methods for SWE (Stelling,. 2022; Brugnano and Casulli,. 2008; Casulli, 2019). The volumes are conserved due to the volume correction equation, but there can be runoff inaccuracies, due to a large time step of 300 s, see Fig. 12b. Therefore, a timestep of 60 s has been chosen for the remaining simulations.

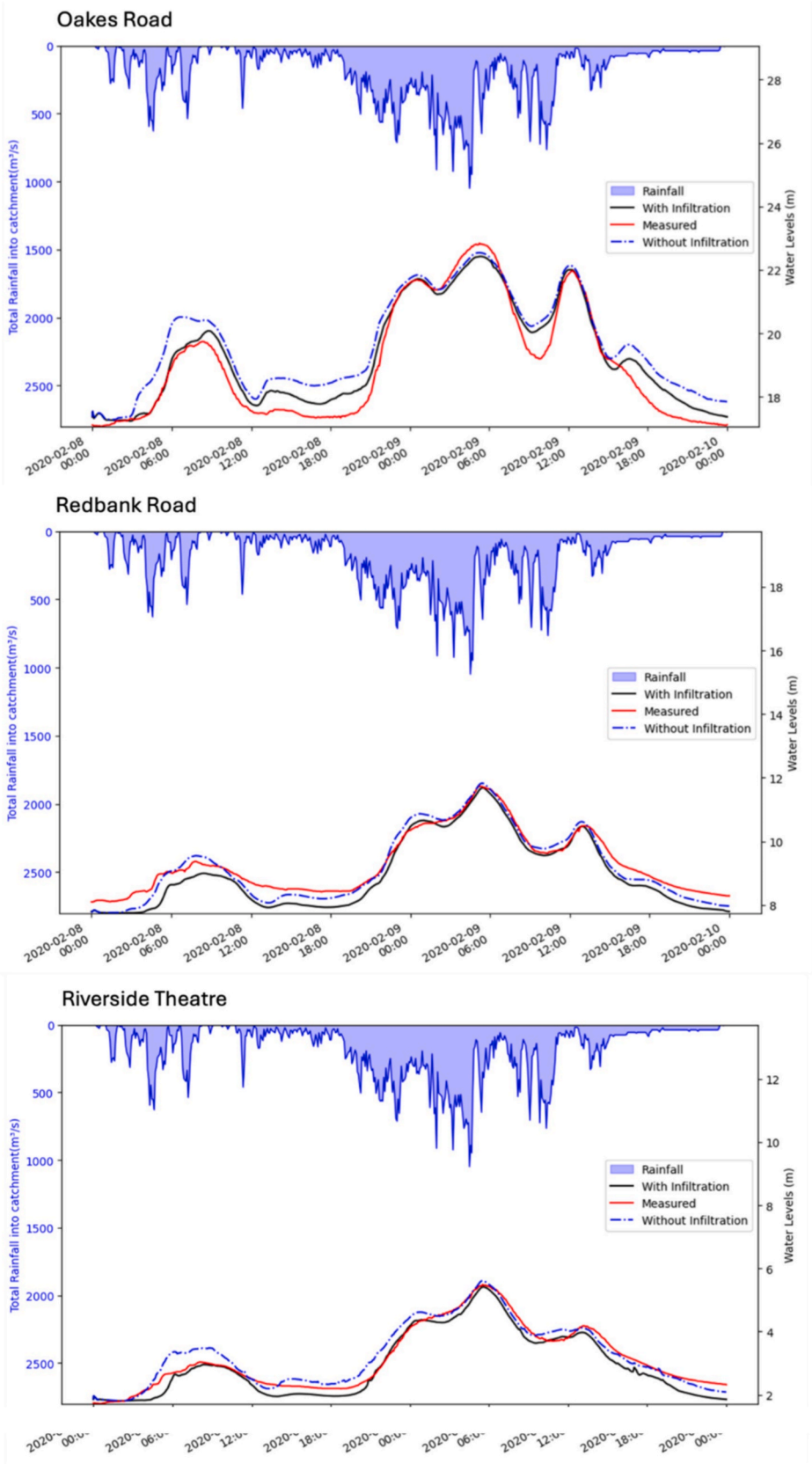

Fig. 13. Simulated Water levels with or without infiltration compared with measurements during February 8 and 9, 2020 at (a) Oakes Road [top], (b) Redbank Road [middle] and (c) Riverside Theatre [bottom] stations.

Table 3
Summary of goodness of fit metrics in different locations with and without infiltration.

	Location	Peak Error	RMSE	NSE	KGE
With infiltration	Riverside Theatre	0.07 *m*	0.26 *m*	0.93	0.92
	Redbank Road	0.05 *m*	0.36 *m*	0.86	0.84
	Oakes Road	0.42 *m*	0.46 *m*	0.93	0.85
Without infiltration	Riverside Theatre	0.12 *m*	0.25 *m*	0.93	0.96
	Redbank Road	0.10 *m*	0.23 *m*	0.94	0.86
	Oakes Road	0.30 *m*	0.78 *m*	0.82	0.78

4.2.3. Historical event

To evaluate the effect of infiltration using DNm-SWE, we simulated a historical rainfall event from February 2020 when about 281 mm rain fell into the catchment within 48 h. The rainfall data from the rain gauges (Fig. 8), were interpolated using Ordinary Kriging method with Gaussian variogram (Kumar Adhikary et al., 2016) using the PyKrige python package (PyKrige — PyKrige 1.7.2 documentation, 2024) across the entire catchment and directly applied as inflow into every computational grid. The model was applied in two modes: (i) assuming an entire impervious domain and (ii) applying Hortons parameters with DNm. The 48-hour simulation takes around 8 min to complete in both modes. Notably, inclusion of infiltration does not result in increased computational times. The simulated water levels are compared with observed water levels and shown in Fig. 13. With infiltration the simulated water levels upstream at Oakes Road (Fig. 13a), show a better fit to the observations than results without infiltration. Infiltration is more dominant in the less urbanized areas upstream. Riverside Theatre (Fig. 13c), which is located at the catchment outlet near Charles Street Weir, is the least sensitive to infiltration. In terms of goodness of fit measures, such as Peak Error (PE), Root Mean Square Error (RMSE), Nash Sutcliffe Efficiency (NSE) (Nash and Sutcliffe, 1970), Kling-Gupta Efficiency (KGE) (Gupta and Kling, 2011), there are mixed results (Table 3). The improvement with infiltration is more noticeable during the first rainfall interval during February 8 event when the infiltration capacity is higher because of antecedent dry conditions, the low rain period between the events and the rising limb due to the February 9 rainfall event.

Despite achieving reasonable fit with observations (with NSE $>$ 0.86 and KGE $>$ 0.83 across the 3 stations) we emphasize that the model parameters are not calibrated. This is visible in the upstream station at Oakes Road (Fig. 13a) where the peak error is more than 0.46 m and in Redbank Road (Fig. 13b) where inclusion of infiltration increases RMSE from 0.23 m to 0.36 m and NSE and KGE are reduced. Water levels are locally affected by nearby control structures. There are 190 hydraulic structures, including weirs and bridges, along the Parramatta River and in the surrounding urban drainage system (Stantec Australia Pty Ltd, 2024) that influence both water levels in the river and discharges into the river. Although the structures have an impact on the water levels at Oakes Road and Redbank Road, we have not included them in the current model setup in the absence of detailed data. The intention of this paper is to demonstrate the effectiveness of the DNm-SWE scheme and the impact of spatiotemporal infiltration rather than the development of a fully calibrated and validated model ready for operational use. It can be a topic of future study. A high-resolution flood map with water depths is greater than 4 cm at 1 m x 1 m, that was generated by the present model configuration is shown in Fig. 14 to illustrate its capability. The runoff from the slopes transfers the water into the river streams, where the maximum water depths occur. The elevated areas become dry shortly after the rain stops, and recovery of infiltration capacity begins immediately after the precipitation ends.

4.2.4. Extreme event

Usually when conducting simulations with extreme rainfall scenarios for flood risk assessment, the surfaces are often considered impervious. However, recent studies (Li, 2022) indicate that the inclusion of dynamic infiltration in hydrodynamic models is important even in flood simulations with extreme events. Here, we consider a 1 in 100 return period 9-hour rainstorm applied across the catchment with 371 mm of rain in 9 h, see Fig. 15. We simulate for 16 h using the same model configuration as described in Section 4.2.2.

Simulated outflow hydrographs show that there is a delay of 40 min in peak runoff when infiltration is considered in comparison to the situation where infiltration is ignored with a 15.5 % decrease in the peak runoff (Fig. 15). Ignoring infiltration reduces the flood extent and there are significant differences for simulated water depths (Fig. 16). The

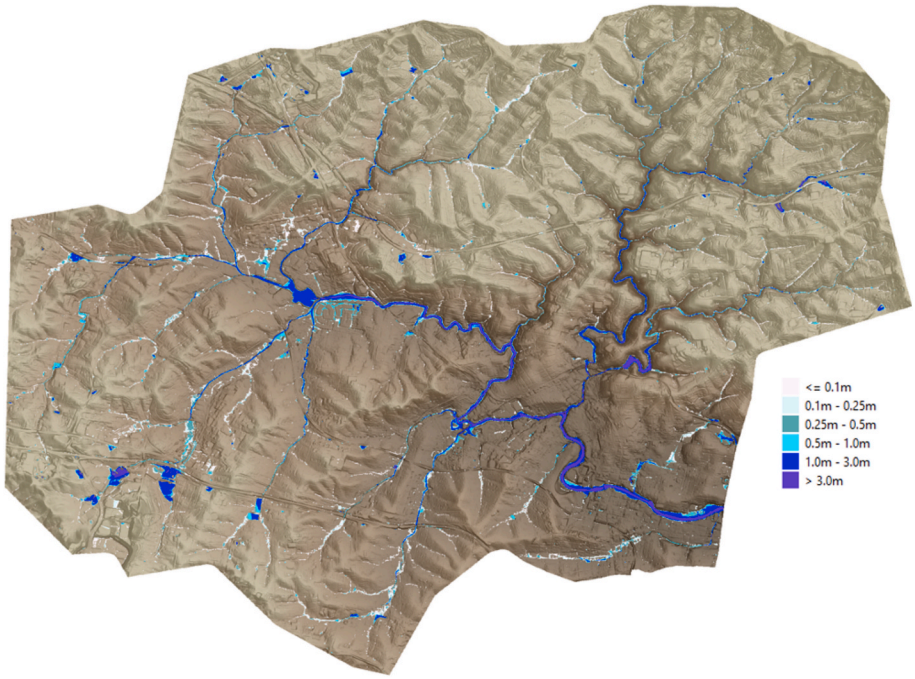

Fig. 14. Simulated flood map with maximum water depths during the February 9, 2020 event.

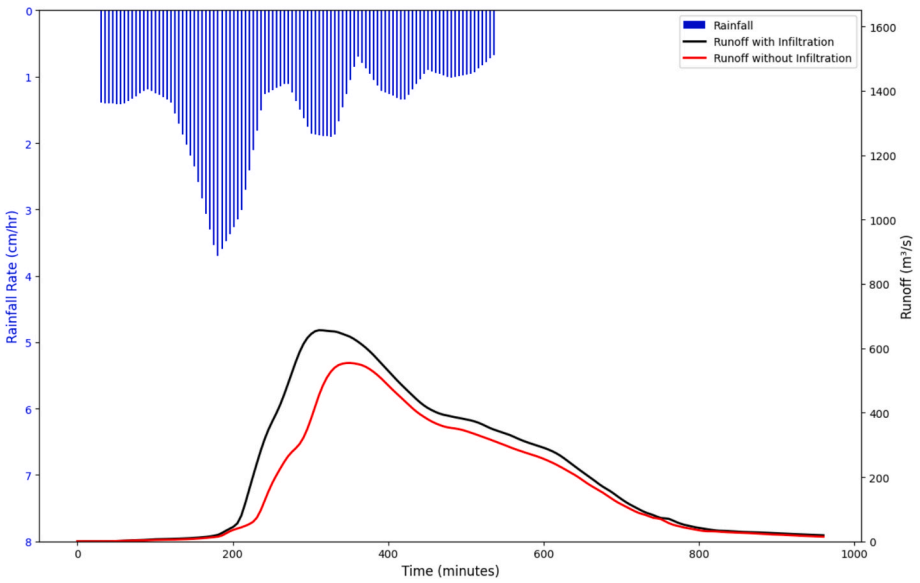

Fig. 15. Simulated runoff from the catchment with and without DNm for infiltration for 1 in 100 year event.

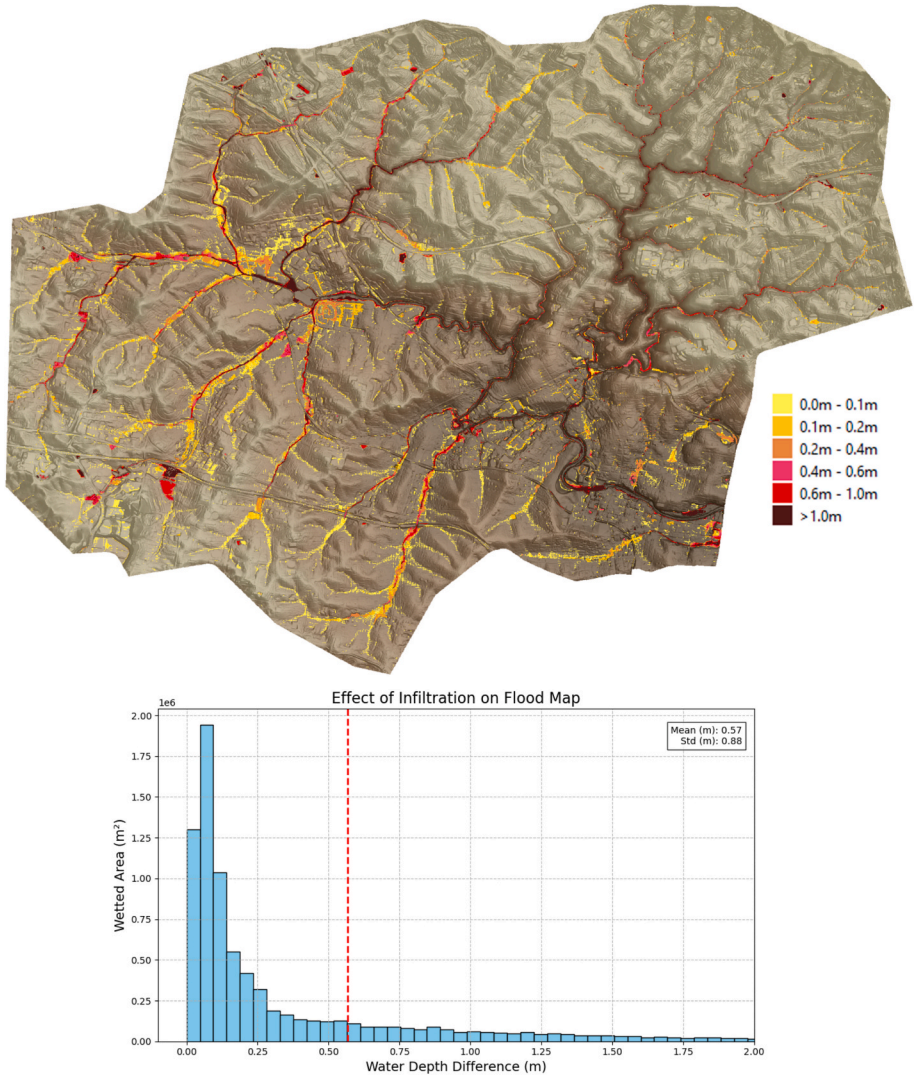

Fig. 16. Comparison of maximum flood water depths with and without infiltration for the 1 in 100 rainfall event.

maximum flood maps show significant differences in the distribution of water depths in the flooded areas, particularly surfaces where infiltration is present in the low-lying urban park areas, also along the river and the waterways, where water depths simulated without infiltration can be higher by 1 m (Fig. 16). In many urban street areas and other depressions in the terrain where water depths are less than 0.25 m without infiltration, inclusion of infiltration reduces flooding. Since the SDB based approach accounts for both rainfall intensity and water depth on the surface – which depends on run-on, it implicitly considers re-infiltration.

The DNm-SWE model can simulate spatiotemporal infiltration and re-infiltration quite efficiently for this extreme event; within 3 min with a single hydrodynamic model framework, unlike other approaches which require coupling between hydrologic and hydrodynamic models (Li, 2022). The SDB implementation of DNm can be easily extended to include other processes such as evapotranspiration avoiding restrictions faced by other implementations (Parnas et al., 2021).

5. Conclusions

In this paper, we started with a novel approach for infiltration that we called Surface Detention Box or SDB. This approach considers not only rain and the infiltration capacity, but also the level of the ponded water. In essence, infiltration depends primarily on the water depth at the surface, while this water depth depends on rain input, infiltration capacity and runoff.

Next three infiltration models, all based on Horton's parameters, were compared. If rain is always larger than the infiltration capacity, then they are all equal. The original Horton's model is insensitive to the actual amount of infiltration. This deficiency is adjusted for by the "modified Horton method". However, there is a deficiency that remains in this model, during rain less than f_c, the infiltration capacity will converge to f_c regardless how small the rainfall is, except for zero rain. This gives an unrealistic discontinuity. For $R< f_c$, DNm converges to a weighted value between f_0 and f_c and depends continuously on R. Therefore, this is more realistic. Recovery of infiltration capacity is an intrinsic property of DNm which follows a time scale according to $\kappa_d = \kappa f_c/f_0$, which can easily be adjusted to a different time scale. Moreover, time integration in DNm is simple and fully linear without the need for iterations. Therefore, this method is our preferred method of Horton parameter-based methods. We have provided both a theoretical analysis and some numerical examples to demonstrate the advantage of DNm for practical infiltration modelling. As noted in literature (Parnas et al.,. 2021), Horton-based methods do not incorporate the effects of evapotranspiration in the regeneration of soil moisture, limiting their applicability for long-term simulations. In contrast, our double-box model approach enables the straightforward integration of additional processes, such as evapotranspiration, providing greater flexibility for extended simulations.

We have implemented DNm as part of a sub-grid algorithm to solve SWE. The algorithm has a corrector that ensures strictly positive water depths $\forall \Delta t > 0$. This enables flooding and drying automatically, which is very valuable for modelling runoff on slopes with infiltration.

We apply the DNm-SWE sub-grid model to the Upper Parramatta River catchment for different rainfall scenarios – synthetic intermittent, historical and extreme events. The numerical simulation results show that the model remains computationally efficient and robust under diverse rainfall conditions with spatially varying Horton's infiltration parameters. Simulations of infiltration have an impact on flood extents, runoff and water depths distributions. Quantitatively, the model could be improved by incorporating hydraulic structures and drainage systems of the urban catchments combined with calibration. However, the primary objective of this paper is to demonstrate a fast and robust approach for 2D rainfall-runoff simulations with detailed DTMs including infiltration. The approach provides a solid foundation for real-time flood predictions, flood risk assessment and evaluation of flood mitigation measures at catchment scale in high-resolution.

CRediT authorship contribution statement

Abhishek Saha: Writing – original draft, Visualization, Validation, Software, Resources, Methodology, Investigation, Funding acquisition, Formal analysis. **Guus Stelling:** Writing – review & editing, Writing – original draft, Validation, Software, Methodology, Formal analysis, Conceptualization. **Cornelis Vuik:** Writing – review & editing, Supervision, Project administration.

Declaration of competing interest

The authors declare that they have no known competing financial interests or personal relationships that could have appeared to influence the work reported in this paper.

Acknowledgements

The first and second authors received financial support from National Research Foundation, Singapore (Grant Number: NRF2017VSG-AT3DCM001-021) and Public Utilities Board, National Water Agency of Singapore (Grant Number: A-0009309-02-00) to develop the model framework. The authors would like to thank Cornelis Dingemanse from Royal Haskoning DHV, Australia for background data related to Upper Parramatta River Catchment characteristics, rainfall events and water levels, and Chris Gooch on behalf of City of Parramatta Council to permit the use of relevant information for this study. The authors are grateful for feedback from the anonymous reviewers.

Appendix A

We illustrate the behaviour of water depths in SDB with analytical solutions for constant values of $R(t)$ and $f_p(t)$, R and f_p. With $t_0 = 0$, we get the following solutions for 3 cases:

$$CaseI : R \geq f_p, \frac{dh}{dt} = R - f_p \rightarrow h(t) = h(0) + \left(R - f_p\right)t \tag{A.1}$$

$$CaseII:\ R < f_p\ ;\ h(0) \geq \eta$$

$$\rightarrow h(t) = \begin{cases} h(0) + \left(R - f_p\right)t, t \leq t^{'}, h(t^{'}) = \eta \\ \left(\eta - \frac{R}{f_p}\eta\right)e^{-\frac{f_p}{\eta}(t-t^{'})} + \frac{R}{f_p}\eta, t > t^{'} \end{cases} \tag{A.2}$$

$$CaseIII: R < f_p, h(0) < \eta \rightarrow h(t) = \left(h(0) - \frac{R}{f_p}\eta\right)e^{-\frac{f_p}{\eta}t} + \frac{R}{f_p}\eta \tag{A.3}$$

Case I will give a constant water depth if $R = f_p$, or a linearly rising water level if $R > f_p$, while $f_i(t) = f_p$, for Case II, the water level will drop at a speed $h_t = R - f_p$, while as soon as $h(t) < \eta$ then this depth will converge rapidly to $\frac{R}{f_p}\eta$, due to the very short time scale of f_p/η. In Case II, this rapid convergence starts immediately. Substitution into (2) gives convergence of the infiltration rate: $f_i(t) = \frac{R}{f_p}\eta\frac{f_p}{\eta} = R$.

In summary, for Case I, the infiltration is given by the infiltration capacity, $f_i = f_p$, while in Case II, the infiltration is given by $f_i = f_p$, if $h(t) \geq \eta$, and converges almost immediately to $f_i = R$, if $h(t) < \eta$.

To estimate the time scale of f_p/η, we take $f_p = 100\left[\frac{mm}{hr}\right]$, $R = 50\left[\frac{mm}{hr}\right]$ and $\eta = 10^{-2}[mm]$. So $f_p/\eta = 10^{-4}\left[\frac{1}{hr}\right] = 1/T_{scale}$ or $.T_{scale} = 0.36\,[s]$

Appendix B

Here we show the equivalence of DNm with Horton for $R(t) > f_p(t)\forall t$, i.e. $f_i = f_p$. Then Eqs. (9)–(11) becomes:

$$\frac{dz}{dt} = \left(1 - \frac{z}{z_{max}}\right)f_0 \tag{B.1}$$

$$z(0) = 0 \rightarrow z(t) = z_{max}\left(1 - e^{-\frac{f_0}{z_{max}}t}\right) = \frac{f_0}{\kappa}(1 - e^{-\kappa t}), \kappa = \frac{f_0}{z_{max}} \tag{B.2}$$

Substituting Eq. (10) and Eq. (B.2) into $f_p(t) = \frac{dz}{dt} + f_g(t)$, we get Eq. (5) again.

This means DNm is equivalent to Horton's model if $R(t) > f_p(t)\forall t$ and $z_{max} = f_0/\kappa$. See also (Li et al., 2015) .

Next, we analyse the recovery of infiltration capacity. We assume that recovery starts if the infiltration into the sub-surface box is less than f_c, often defined as the hydraulic conductivity of saturated soil. For this purpose, we choose $R = \alpha f_c, 0 \leq \alpha \leq 1$. This implies that $f_i = \alpha f_c$. Eq. (9) and Eq. (10) become

$$\frac{dz}{dt} + \frac{f_c}{z_{max}}z = \alpha f_c, z(t_r) = z_{max} \tag{B.3}$$

Where we have assumed that at a moment in time, given by t_r, that recovery of infiltration capacity starts, we have $f_p = f_c$. The solution of (B.3) reads:

$$z(t) = \alpha z_{max} + (1 - \alpha)z_{max}e^{-\frac{f_c}{z_{max}}(t - t_r)} \tag{B.4}$$

Substitution of Eq. (B.4) into Eq. (11) yields:

$$f_r(t) = \alpha f_c + (1 - \alpha)f_0 + \left(f_c - f_0\right)\left((1 - \alpha)e^{-\frac{f_c}{z_{max}}(t - t_r)}\right) \tag{B.5}$$

For $\alpha = 0$ we get Eq. (8) with $\kappa_d = \frac{f_c}{z_{max}} = \frac{f_c}{f_0}\kappa$. Since $f_c \ll f_0$; this seems to be a reasonable assumption. This is an inherent characteristic of DNm. If required, we can explicitly define other recovery time scales with the specification of an additional parameter and an adjustment of Eq. (10), based on the criterium $f_i < f_c$. Another aspect of Eq. (B.5) is that for low steady precipitation with, $R \leq f_c \rightarrow 0 \leq \alpha \leq 1$, the infiltration capacity for $t \rightarrow \infty$ will be a weighted average between f_c and f_0 given by:

$$\underset{t\rightarrow\infty}{\mathrm{Lim}} f_p(t) = (1 - R/f_c)f_0 + R \tag{B.6}$$

Hence, for DNm recovery of infiltration capacity depends continuously on $R < f_c$.

Appendix C

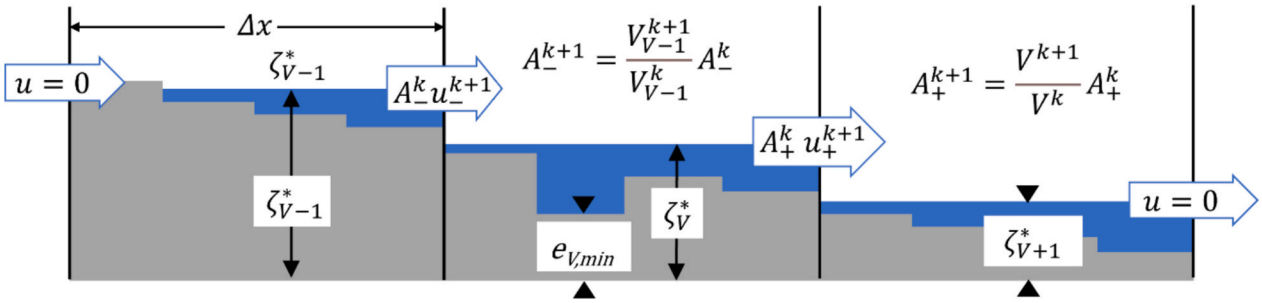

Fig. 3.1. 1D example of 3 volumes with sub-grid

Consider a simple 1D sub-grid, see Fig. 3.1. For this grid we describe the solution procedure based on Eqs. (17)–(22) via the steps **A** to **H.** First initialize all the variables at $t = 0$. Then compute the time steps from $k = 1$ until $k = T/\Delta t$as follows:

A: Compute wet cross sections (Stelling,. 2022), bottom friction coefficients, and advection terms (Kramer and Stelling, 2008) then, based on Eq. (17) assemble the coefficients of the momentum equations:

$$\mathbf{A}: \begin{cases} u_{-}^{k+1} = c_{-}^{k}\left(\zeta_{V-1}^{*} - \zeta_{V}^{*}\right) + D_{-}^{'} \\ u_{+}^{k+1} = c_{+}^{k}\left(\zeta_{V}^{*} - \zeta_{V+1}^{*}\right) + D_{+}^{'} \end{cases}$$

where:

$$c_{-,+}^{k} = g\Delta t \Big/ \left(\Delta x\left(1 + \Delta t c_{f_{-,+}}^{k}\left\|u_{-,+}^{k}\right\| \Big/ h_{-,+}^{k}\right)\right),$$

$D_{-,+}^{'} = u_{-,+}^{'} \Big/ \left(1 + \Delta t c_{f_{-,+}}^{k}\left\|u_{-,+}^{k}\right\| / h_{-,+}^{k}\right)$, $u_{-,+}^{'}$ includes advection, (Kramer and Stelling, 2008).

B: Compute the coefficients of the prediction/continuity equation, Eq. (18):

$$\mathbf{B}: \begin{cases} a_{V-1}^{k}\zeta_{V-1}^{*} + A_{-}^{k}\ u_{-}^{k+1} = C_{V-1}^{k} \\ a_{V}^{k}\zeta_{V}^{*} - A_{-}^{k}\ u_{-}^{k+1} + A_{+}^{k}u_{+}^{k+1} = C_{V}^{k} \\ a_{V+1}^{k}\zeta_{V+1}^{*} - A_{+}^{k}u_{+}^{k+1} = C_{V+1}^{k} \end{cases}$$

where:

$$a_{V+n}^{k} = \frac{S_{V+n}^{k}}{\Delta t},$$

$$C_{V+n}^{k} = S_{V+n}^{k}\frac{\zeta_{V+n}^{k}}{\Delta t} + S_{V+n,max}\left(R_{V}^{k} - \min\left(\frac{V^{k}}{\Delta t S_{max_{V+n}}} + R_{V+n}^{k}, f_{P_{V+n}}^{k}\right)\right)$$

$$n = -1, 0, 1$$

C: Substitute **A** into **B** to eliminate u_{-}^{k+1} and u_{+}^{k+1} from **B** to get **C:**

$$\mathbf{C}: \begin{bmatrix} a_{V-1}^{k} + A_{-}^{k}\ c_{-}^{k} & -A_{-}^{k}\ c_{-}^{k} & 0 \\ -A_{-}^{k}\ c_{-}^{k} & a_{V}^{k} + A_{-}^{k}\ c_{-}^{k} + A_{+}^{k}c_{+}^{k} & -A_{+}^{k}c_{+}^{k} \\ 0 & -A_{+}^{k}c_{+}^{k} & a_{V+1}^{k} + A_{+}^{k}c_{+}^{k} \end{bmatrix} \begin{bmatrix} \zeta_{V-1}^{*} \\ \zeta_{V}^{*} \\ \zeta_{V+1}^{*} \end{bmatrix} = \begin{bmatrix} C_{V-1}^{k} - b_{-}^{k}D_{-}^{'} \\ C_{V}^{k} + b_{-}^{k}D_{-}^{'} - b_{+}^{k}D_{+}^{'} \\ C_{V+1}^{k} + b_{+}^{k}D_{+}^{'} \end{bmatrix}$$

Solve **C**, a symmetric and positive definite system, with preconditioned CG (Golub and Van Loan, 2013), then substitute $\left(\zeta_{V-1}^{*}, \zeta_{V}^{*}, \zeta_{V+1}^{*}\right)$ into **A** to compute $u_{-,+}^{k+1}$, $Q_{-,+}^{*}$

D: Assemble the volume correction equation based on Eq. (19), while assuming$u_{-,+}^{k+1} > 0$ (that implies that for Volume V: $u_{-}^{k+1} = u_{I(nput)}^{k+1}$ and $u_{+}^{k+1} = u_{O(utput)}^{k+1}$) to obtain:

$$\boldsymbol{D}: \begin{bmatrix} \frac{1}{\Delta t} + \frac{Q_-^* + \overline{\overline{Q}}_{i_{V-1}}^*}{V_{V-1}^k} 00 \frac{Q_-^*}{V_{V-1}^k} \frac{1}{\Delta t} + \frac{Q_+^* + \overline{\overline{Q}}_{i_V}^*}{V^k} 00 \frac{Q_-^*}{V^k} \frac{1}{\Delta t} + \frac{\overline{\overline{Q}}_{i_{V+1}}^*}{V_{V+1}^k} \end{bmatrix} \begin{bmatrix} V_{V-1}^{k+1} \\ V^{k+1} \\ V_{V+1}^{k+1} \end{bmatrix} = \begin{bmatrix} \frac{V_{V-1}^k}{\Delta t} + Q_{R_{V-1}}^k - \overline{Q}_{i_{V-1}}^* \\ \frac{V^k}{\Delta t} + Q_{R_V}^k - \overline{Q}_{i_V}^* \\ \frac{V_{V+1}^k}{\Delta t} + Q_{R_{V+1}}^k - \overline{Q}_{i_{V+1}}^* \end{bmatrix}$$

where:

$$\overline{Q}_{i_{V+n}}^* = \begin{cases} S_{V+n,max} f_{p_{V+n}}^k, R_{V+n}^k \geq f_{p_{V+n}}^k \\ 0, R_{V+n}^k < f_{p_{V+n}}^k \end{cases}$$

$$\overline{\overline{Q}}_{i_V}^* = \begin{cases} 0, R_{V+n}^k \geq f_{p_{V+n}}^k \\ S_{V+n,max} f_{p_{V+n}}^k, R_{V+n}^k < f_{p_{V+n}}^k \end{cases}$$

$\overline{Q}_{i_{V+n}}^*$ and $\overline{\overline{Q}}_{i_V}^*$ are the actual implementation of the SDB in the Volume Correction Equation.

D implies a diagonally dominant matrix, to be solved efficiently by Gauss-Seidel's method (Varga, 2000), with iterations in alternating sweep directions. For a strictly lower diagonal matrix this method gets the solution in one sweep. Due to our assumption of velocities all in the same direction, the solution of our example is as follows:

$$V_{V-1}^{k+1} = \frac{V_{V-1}^k + \Delta t\left(Q_{R_{V-1}}^k - \overline{Q}_{i_{V-1}}^*\right)}{1 + \Delta t\left(Q_+^* + \overline{\overline{Q}}_{i_{V-1}}^*\right)/V_{V-1}^k} V^{k+1} = \frac{V^k + \Delta t\left(Q_-^* V_{V-1}^{k+1}/V_{V-1}^k + Q_{R_V}^k - \overline{Q}_{i_V}^*\right)}{1 + \Delta t\left(Q_+^* + \overline{\overline{Q}}_{i_V}^*\right)/V^k} V_{V+1}^{k+1} = \frac{V_{V+1}^k + \Delta t\left(Q_+^* V^{k+1}/V^k + Q_{R_{V+1}}^k - \overline{Q}_{i_{V+1}}^*\right)}{1 + \Delta t \overline{\overline{Q}}_{i_{V-1}}^*/V_{V+1}^k}$$

Note that all nominators and denominators are positive. That means that all volumes and water depths are positive as well. This observation holds also for Eq. (19) in general (Stelling,. 2022).

E: compute $\zeta_{V+n}^{k+1}, n = -1, 0, 1$ from Eq. (20) via a look up table.

F: compute $z_{V+n}^{k+1}, n = -1, 0, 1$ from Eq. (21)

$$\mathbf{F}: z_{V+n}^{k+1} = \frac{z_{V+n}^k + \Delta t f_{iV+n}^{k+1}}{1 + \Delta t f_{cV+n} z_{V+n}^{k+1}/z_{maxV+n}}, f_{iV+n}^{k+1} = \begin{cases} f_{p_{V+n}}^k, R_{V+n}^k \geq f_{p_{V+n}}^k \\ f_{p_{V+n}}^k V_{V+n}^{k+1}/V_{V+n}^k, R_{V+n}^k < f_{p_{V+n}}^k \end{cases}; n = -1, 0, 1$$

G: compute $f_{p_{V+n}}^k, n = -1, 0, 1$ from Eq. (22)

$$\mathbf{H}: f_{p_{V+n}}^{k+1} = f_{cV+n} + \left(1 - \frac{z_{V+n}^{k+1}}{z_{maxV+n}}\right)\left(f_{0V+n} - f_{cV+n}\right), n = -1, 0, 1$$

H: if k equals $T/\Delta t$ then stop, else update all variables with index k and go to **A**

Data availability

The authors do not have permission to share data.

References

Aron, G., Mar. 1992. Adaptation of horton and scs infiltration equations to complex storms. J. Irrig. Drain. Eng., 118 (2), 275–284. https://doi.org/10.1061/(ASCE)0733-9437(1992)118:2(275).

Artiglieri, P., Curulli, G., Coscarella, F., Ferraro, D.A., Macchione, F., 2025. Performance of HEC-RAS v6.5 at basin scale for calculating the flow hydrograph: comparison with TUFLOW. Nat. Hazards 1–14. https://doi.org/10.1007/s11069-025-07170-x.

Assouline, S., Apr. 2013. Infiltration into soils: Conceptual approaches and solutions. Water Resour. Res., 49 (4), 1755–1772. https://doi.org/10.1002/wrcr.20155.

Aureli, F., Prost, F., Vacondio, R., Dazzi, S., Ferrari, A., 2020. A GPU-Accelerated Shallow-Water Scheme for Surface Runoff Simulations. Water 12 (3), 637. https://doi.org/10.3390/w12030637.

Australian Soil Classification (ASC) soil type map of NSW - SEED. Accessed: Feb. 23, 2024. [Online]. Available: https://datasets.seed.nsw.gov.au/dataset/australian-soil-classification-asc-soil-type-map-of-nsweaa10.

Bates, P.D., 2000. Development and testing of a subgrid-scale model for moving-boundary hydrodynamic problems in shallow water. Hydrol. Process., 14 (11–12), 2073–2088. https://doi.org/10.1002/1099-1085(20000815/30)14:11/12<2073::AID-HYP55>3.0.CO;2-X.

Bauer, S.W., 1974. A modified horton equation for infiltration during intermittent rainfall. Hydrol. Sci. J. ISSN 219–225.

Brugnano, L., Casulli, V., 2008. Iterative solution of piecewise linear systems. SIAM J. Sci. Comput. 30 (1), 463–472. https://doi.org/10.1137/070681867.

Casulli, V., 2009. A high-resolution wetting and drying algorithm for free-surface hydrodynamics. Int. J. Numer. Methods Fluids 60, 391–408.

Casulli, V., May 2019. Computational grid, subgrid, and pixels. Int. J. Numer. Methods Fluids 90 (3), 140–155. https://doi.org/10.1002/fld.4715.

Chanson, H., 2004. The hydraulics of open channel flow, 2nd ed. Butterworth-Heinemann, Oxford.

Chu, C., Mariño, M.A., 2005. Determination of ponding condition and infiltration into layered soils under unsteady rainfall. J. Hydrol., 313 (3–4), 195–207. https://doi.org/10.1016/j.jhydrol.2005.03.002.

Corradini, C., Melone, F., Smith, R.E., Oct. 1994. Modeling infiltration during complex rainfall sequences. Water Resour. Res., 30 (10), 2777–2784. https://doi.org/10.1029/94WR00951.

Diskin, M.H., Nazimov, N., 1995. Linear reservoir with feedback regulated inlet as a model for the infiltration process. J. Hydrol., 172 (1–4), 313–330. https://doi.org/10.1016/0022-1694(95)02709-X.

Diskin, M.H., Nazimov, N., Apr. 1996. Ponding time and infiltration capacity variation during steady rainfall. J. Hydrol., 178 (1–4), 369–380. https://doi.org/10.1016/0022-1694(95)02798-X.
Fernández-Pato, J., Caviedes-Voullième, D., García-Navarro, P., May 2016. Rainfall/runoff simulation with 2D full shallow water equations: Sensitivity analysis and calibration of infiltration parameters. J. Hydrol. 536, 496–513. https://doi.org/10.1016/j.jhydrol.2016.03.021.
Fernández-Pato, J., Gracia, J.L., García-Navarro, P., Jul. 2018. A fractional-order infiltration model to improve the simulation of rainfall/runoff in combination with a 2D shallow water model. J. Hydroinform. 20 (4), 898–916. https://doi.org/10.2166/hydro.2018.145.
Flash Flood Forecasting Parramatta, Sydney, Nelen & Schuurmans. Accessed: Jan. 21, 2024. [Online]. Available: https://nelen-schuurmans.nl/en/case/flash-flood-forecasting-parrramatta-sydney/.
Flood Warning Service | City of Parramatta. Accessed: Nov. 22, 2024. [Online]. Available: https://www.cityofparramatta.nsw.gov.au/environment/floodsmart-parramatta/flood-warning-service.
Fujimura, K., Iseri, Y., Kanae, S., Murakami, M., Sep. 2014. Identification of low-flow parameters a using hydrological model in selected mountainous basins in Japan. Proc. Int. Assoc. Hydrol. Sci., 364, 51–56. https://doi.org/10.5194/piahs-364-51-2014.
Fujimura, K., Iseri, Y., Kanae, S., Murakami, M., Jun. 2015. Generalization of parameters in the storage–discharge relation for a low flow based on the hydrological analysis of sensitivity. Proc. Int. Assoc. Hydrol. Sci., 371, 69–73. https://doi.org/10.5194/piahs-371-69-2015.
Gabellani, S., Silvestro, F., Rudari, R., Boni, G., Dec. 2008. General calibration methodology for a combined Horton-SCS infiltration scheme in flash flood modeling. Nat. Hazards Earth Syst. Sci., 8 (6), 1317–1327. https://doi.org/10.5194/nhess-8-1317-2008.
García-Feal, O., González-Cao, J., Gómez-Gesteira, M., Cea, L., Domínguez, J.M., Formella, A., Oct. 2018. An accelerated tool for flood modelling based on iber. Water 10 (10), 1459. https://doi.org/10.3390/w10101459.
Geoscience Australia Portal. Accessed: Jan. 19, 2024. [Online]. Available: https://portal.ga.gov.au/.
Godara O, Bruland, Alfredsen K, "Comparison of two hydrodynamic models for their rain-on-grid technique to simulate flash floods in steep catchment," Front. Water, vol. 6, p. 1384205, May 2024, doi: 10.3389/frwa.2024.1384205.
Golub, G.H., Van Loan, C.F., 2013. Matrix computations, Fourth edition. The Johns Hopkins University Press, Baltimore.
Green, I.R.A., 1986. An explicit solution of the modified Horton equation. J. Hydrol. 83, 23–27.
Green, W., Ampt, G.A., 1911. Studies on Soil Phyics. J. Agric. Sci., 4 (1), 1–24. https://doi.org/10.1017/S0021859600001441.
Gülbaz, O.S., Boyraz, U., Kazezyilmaz-Alhan, C.M., Feb. 2020. Investigation of overland flow by incorporating different infiltration methods into flood routing equations. Urban Water J., 17 (2), 109–121. https://doi.org/10.1080/1573062X.2020.1748206.
Gupta HV, Kling H, "On typical range, sensitivity, and normalization of mean squared error and nash–sutcliffe efficiency type metrics," Water Resour. Res., vol. 47, no. 10, p. 2011WR010962, Oct. 2011, doi: 10.1029/2011WR010962.
Hodges, B.R., 2015. Representing hydrodynamically important blocking features in coastal or riverine lidar topography. Nat. Hazards Earth Syst. Sci., 15, 1011–1023. https://doi.org/10.5194/nhess-15-1011-2015.
Horton RE, "An approach toward a physical interpretation of infiltration-capacity," Soil Sci. Soc. Am. J., vol. 5, no. C, pp. 399–417, Jan. 1941, doi: 10.2136/sssaj1941.03615995000500C0075x.
Jiang YC, Zevenbergen, Ma Y, "Urban pluvial flooding and stormwater management: a contemporary review of China's challenges and 'sponge cities' strategy," Environ. Sci. Policy, vol. 80, pp. 132–143, Feb. 2018, doi: 10.1016/j.envsci.2017.11.016.
Karahan, G., Pachepsky, Y., Jun. 2022. Parameters of infiltration models affected by the infiltration measurement technique and land-use. Rev. Bras. Ciênc. Solo 46, e0210147. https://doi.org/10.36783/18069657rbcs20210147.
Kennedy, A.B., Wirasaet, D., Begmohammadi, A., Sherman, T., Bolster, D., Dietrich, J.C., 2019. Subgrid theory for storm surge modeling. Ocean Modelling 144. https://doi.org/10.1016/j.ocemod.2019.101491.
Kramer, S.C., Stelling, G.S., 2008. "A conservative unstructured scheme for rapidly varied flows,". Int. J. Numer. Methods Fluids. https://doi.org/10.1002/fld.1722.
Kumar Adhikary S, Muttil N, Yilmaz AG, "Ordinary kriging and genetic programming for spatial estimation of rainfall in the Middle Yarra River catchment, Australia," Hydrol. Res., vol. 47, no. 6, pp. 1182–1197, Dec. 2016, doi: 10.2166/nh.2016.196.
Lambert, J.D., 1999. Numerical methods for ordinary differential systems: the initial value problem, Repr. Wiley, Chichester.
Li, J., Wang, Z., Liu, C., 2015. A combined rainfall infiltration model based on Green–Ampt and SCS-curve number. Hydrol. Process., 29 (11), 2628–2634. https://doi.org/10.1002/hyp.10379.
Li, Z., et al., Sep. 2022. Can re-infiltration process be ignored for flood inundation mapping and prediction during extreme storms? a case study in Texas Gulf Coast region. Environ. Model. Softw., 155, 105450. https://doi.org/10.1016/j.envsoft.2022.105450.
Michel C, Andréassian V, Perrin C, "Soil conservation service curve number method: how to mend a wrong soil moisture accounting procedure?" Water Resour. Res., vol. 41, no. 2, p. 2004WR003191, Feb. 2005, doi: 10.1029/2004WR003191.
Mishra, S.K., Singh, V.P., 2003. Soil conservation service curve number (SCS-CN) methodology. Springer Science+Business Media, Dordrecht, [Netherlands].
Van Der Molen, W.H., Dec. 1986. A predictor-corrector solution of the modified Horton equation. J. Hydrol., 89 (1–2), 165–167. https://doi.org/10.1016/0022-1694(86)90150-2.
Morbidelli, R., Corradini, C., Saltalippi, C., Flammini, A., Dari, J., Govindaraju, R.S., Dec. 2018. Rainfall Infiltration Modeling: A Review. Water 10 (12), 1873. https://doi.org/10.3390/w10121873.
Nash, J.E., Sutcliffe, J.V., 1970. River flow forecasting through conceptual models part I — A discussion of principles. J. Hydrol., 10 (3), 282–290. https://doi.org/10.1016/0022-1694(70)90255-6.
Ni, Y., Cao, Z., Liu, Q., Liu, Q., 2020. A 2D hydrodynamic model for shallow water flows with significant infiltration losses. Hydrol. Process., 34 (10), 2263–2280. https://doi.org/10.1002/hyp.13722.
Van Ormondt, M., Leijnse, T., de Goede, R., Nederhoff, K., van Dongeren, A., 2025. Subgrid corrections for the linear inertial equations of a compound flood model – a case study using SFINCS 2.1.1 Dollerup release. Geosci. Model Dev., 18, 843–861. https://doi.org/10.5194/gmd-18-843-2025.
Parnas, F.E.Å., Abdalla, E.M.H., Muthanna, T.M., Feb. 2021. Evaluating three commonly used infiltration methods for permeable surfaces in urban areas using the SWMM and STORM. Hydrol. Res., 52 (1), 160–175. https://doi.org/10.2166/nh.2021.048.
Patankar SV, Numerical heat transfer and fluid flow, 1st ed. CRC Press, 2018, doi: 10.1201/9781482234213.
Pearlmutter, D., et al., Aug. 2021. Closing water cycles in the built environment through nature-based solutions: the contribution of vertical greening systems and green roofs. Water 13 (16), 2165. https://doi.org/10.3390/w13162165.
Peng, F., Hao, X., Chai, F., Mar. 2023. A GPU-accelerated two-dimensional hydrodynamic model for unstructured grids. Water 15 (7), 1300. https://doi.org/10.3390/w15071300.
PyKrige — PyKrige 1.7.2 documentation. Accessed: Feb. 27, 2024. [Online]. Available: https://geostat-framework.readthedocs.io/projects/pykrige/en/stable/.
Rawls, W.J., Brakensiek, D.L., Miller, N., 1983. Green-ampt infiltration parameters from soils data. J. Hydraul. Eng., 109 (1), 62–70. https://doi.org/10.1061/(ASCE)0733-9429(1983)109:1(62).
Richards, L.A., 1931. Capillary conduction of liquids through porous mediums. Physics 1 (5), 318–333. https://doi.org/10.1063/1.1745010.
Ross, C.W., Prihodko, L., Anchang, J., Kumar, S., Ji, W., Hanan, N.P., 2018. Global hydrologic soil groups (HYSOGs250m) for curve number-based runoff modeling. ORNL Distributed Active Archive Center. https://doi.org/10.3334/ORNLDAAC/1566.
Rossman LA, "Storm Water Management Model User's Manual Version 5.1," U.S. Environmental Protection Agency, User's Manual EPA-600/R-14/413b, 2015.
Ruheili, A.A., Dahm, R., Radke, J., 2019. Wadi flood impact assessment of the 2002 cyclonic storm in Dhofar, Oman under present and future sea level conditions. J. Arid Environm. 165, 73–80. https://doi.org/10.1016/j.jaridenv.2019.04.002.
Shao, Q., Baumgartl, T., Feb. 2016. Field evaluation of three modified infiltration models for the simulation of rainfall sequences. Soil Sci 181 (2). https://doi.org/10.1097/SS.0000000000000136.
Shun, C.F.K., 2018. 'Sponge City' in China—a breakthrough of planning and flood risk management in the urban context. Land Use Policy 76, 772–778.
Song, J., et al., Sep. 2023. Evaluation of permeable brick pavement system infiltration performance via experiment and SWMM. J. Irrig. Drain. Eng., 149 (9), 04023019. https://doi.org/10.1061/JIDEDH.IRENG-10057.
Stantec Australia Pty Ltd, "Parramatta River Flood Study," City of Parramatta Council, Parramatta, NSW, 59916074/304600102, Jun. 2024.
Stelling, G.S., Duinmeijer, S.P.A., 2003. A staggered conservative scheme for every Froude number in rapidly varied shallow water flows. Int. J. Numer. Methods Fluids 43, 1329–1354.
Stelling, G.S., 2012. "Quadtree flood simulations with sub-grid digital elevation models". Proc. Inst. Civ. Eng. - Water Manag., 165 (10), 567–580. https://doi.org/10.1680/wama.12.00018.
Stelling, G.S., Oct. 2022. Boosted robustness of semi-implicit subgrid methods for shallow water flash floods in hills. Comput. Fluids 247, 105645. https://doi.org/10.1016/j.compfluid.2022.105645.
US Army Corps of Engineers 2025 HEC-RAS. Available: https://www.hec.usace.army.mil/software/hec-ras/.
Vallés, P., 2024. A 2D shallow water flow model with 1D internal boundary condition for subgrid-scale topography. Adv. Water Res. 189.
R. S. Varga, Matrix iterative analysis, revised and extended edition. Springer, 2000, e-ISBN 978-3-642-05156-2, doi: 10.1007/978-3-642-05156-2.
Verma, S.C., Sep. 1982. Modified Horton's infiltration equation. J. Hydrol., 58 (3–4), 383–388. https://doi.org/10.1016/0022-1694(82)90047-6.
Viessman, W., Lewis, G.L., 2003. Introduction to hydrology, 5th ed. Prentice Hall, Upper Saddle River, NJ.
Volp, N.D., van Prooijen, B.C., Stelling, G.S., 2013. A finite volume approach for shallow water flow accounting for high-resolution bathymetry and roughness data. Water Resour. Res., 49, 4126–4135. https://doi.org/10.1002/wrcr.20324.
Wang, H.V., Loftis, D., Liu, Z., Forrest, D., Zhang, J., 2014. The storm surge and sub-grid inundation modeling in new york city during hurricane sandy. J. Mar. Sci. Eng., 2, 226–246. https://doi.org/10.3390/jmse2010226.
Wang, J., Song, J., Lin, H., Peng, L., Li, K., Wang, Z., Sep. 2021. Comparison of infiltration models to describe infiltration characteristics of bioretention. J. Hydro-Environ. Res., 38, 35–43. https://doi.org/10.1016/j.jher.2021.08.002.
Wang, N., Chu, X., Oct. 2020. Revised Horton model for event and continuous simulations of infiltration. J. Hydrol., 589, 125215. https://doi.org/10.1016/j.jhydrol.2020.125215.
Water Data Online: Water Information: Bureau of Meteorology. Accessed: Feb. 14, 2024. [Online]. Available: http://www.bom.gov.au/waterdata/.

WaterInsights - WaterNSW. Accessed: Feb. 14, 2024. [Online]. Available: https://waterinsights.waternsw.com.au/download.

WBM Pty Ltd, TUFLOW users manual 2025. WBM Oceanics, Australia. Available: https://docs.tuflow.com/classic-hpc/manual/2025.0/.

Yang, M., Zhang, Y., Pan, X., Jul. 2020. Improving the Horton infiltration equation by considering soil moisture variation. J. Hydrol., 586, 124864. https://doi.org/10.1016/j.jhydrol.2020.124864.

Yang, Y., Shao, Z., Xu, X., Liu, D., Sep. 2023. Impact of storm characteristics on infiltration dynamics in sponge cities using SWMM. Water 15 (19), 3367. https://doi.org/10.3390/w15193367.

Y. C. Hsu, G. Prinsen, L. Bouaziz, Y. J. Lina, and R. Dahm, "An Investigation of DEM Resolution Influence on Flood Inundation Simulation," in 12th International Conference on Hydroinformatics, HIC 2016, Procedia Engineering, vol. 154, pp. 826–834, 2016, doi: 10.1016/j.proeng.2016.07.435.